日本磁気学会
ISSN 2432-0250
Journal of the Magnetics Society of Japan
Electronic Journal URL: https://www.jstage.jst.go.jp/browse/msjmag

Vol.44 No.4 2020

Journal

JOURNAL OF THE MAGNETICS SOCIETY OF JAPAN

Vol.44 No.4 2020

日本磁気学会

ISSN 2432-0250

HP: http://www.magnetics.jp/ e-mail: msj@bj.wakwak.com
Electronic Journal: http://www.jstage.jst.go.jp/browse/msjmag

Journal of the Magnetics Society of Japan
Vol. 44, No. 4

Electronic Journal URL: https://www.jstage.jst.go.jp/browse/msjmag

CONTENTS

J. Magn. Soc. Jpn., **44**, 87-90 (2020)

Letter

Iron Losses and Magnetic-Hysteresis Properties Under GaN Inverter Excitation at High-Frequencies

A. Yao*, R. Moriyama, and T. Hatakeyama
Department of Electrical and Computer Engineering, Toyama Prefectural University, *5180, Kurokawa, Imizu 939-0398, Japan*
*Current address: Advanced Power Electronics Research Center, National Institute of Advanced Industrial Science and Technology (AIST), *16-1, Tsukuba 305-8560, Japan*

Many researchers have investigated the magnetic properties of magnetic cores in order to reduce iron losses in power-electronic systems. Wide bandgap power-semiconductor devices (silicon carbide (SiC) and gallium nitride (GaN)) with high-speed switching characteristics have been studied. Here, we examine the iron losses and magnetic *B-H* loop properties of magnetic materials under excitation with a GaN inverter at high carrier frequencies on the order of MHz. We find that the magnetic *B-H* loops include minor loops due to the magnetic materials even at such high carrier frequencies. We show that the iron losses increase at high carrier frequencies due to distortions of the voltage waveform.

Key words: Iron loss, high-frequency, *B-H* loop, GaN, inverter, high-speed switching

1 Introduction

An inverter is the component of a power-electronic system that changes direct current (DC) to alternating current (AC). A pulse-width modulation (PWM) inverter can be used to obtain variable voltages with variable frequencies and to control the speed and torque in a motor system. In a motor system that has a PWM inverter, the time-harmonic components induce complex magnetic *B-H* loops in the motor core, which is made of soft magnetic materials[1–19]. Due to these time-harmonic components, the iron losses in soft magnetic cores fed by a PWM inverter increase by about 10%-50% compared to the case of sinusoidal excitation[5]. It is therefore important to understand the basic iron-loss properties of magnetic cores under PWM inverter excitation. This study aims to examine the iron losses and magnetic *B-H* loop properties of magnetic cores fed by a PWM inverter at high carrier frequencies.

In recent years, next-generation (wide bandgap) power-semiconductor devices based on silicon carbide (SiC) and gallium nitride (GaN) have been developed and studied. These semiconductor devices have the advantages of high-temperature and high-voltage operation, high-speed switching, and low on-resistance[13,14]. One reason for the active research on these SiC and GaN devices is their high-speed switching characteristics[13,14]. For example, it is considered that, by increasing the carrier frequency of the inverter excitation, an excitation wave that is closer to a sinusoidal waveform can be obtained, and the iron losses of the magnetic cores can be reduced. In addition, understanding the iron-loss properties of magnetic cores under PWM inverter excitation at high carrier frequencies is also useful for motor-core design for high speeds. Depending on the carrier frequency, it is therefore important to understand the basic properties of magnetic materials for use with inverters that employ SiC and GaN devices.

Previous studies have reported iron losses and magnetic *B-H* loop properties of magnetic materials excited by GaN inverters with carrier frequencies on the order of kHz[7,8]. They achieved the inverter excitation with dead time[7,8]. Since ringing noise appeared in these studies, however, the investigators were unable to measure clearly the minor loops of the magnetic materials[7,8]. The next step is therefore to investigate the iron losses and clear magnetic *B-H* hysteresis loop properties under PWM inverter excitation with carrier frequencies on the order of MHz and without dead time.

This study focuses on the experimental determination of iron losses and magnetic *B-H* loop properties of magnetic materials under inverter excitation at high carrier frequencies on the order of MHz. We evaluated the iron losses of a ring core made of magnetic materials and fed by a PWM inverter with a GaN field-effect transistor (GaN-FET). We discuss the iron losses and magnetic *B-H* loop properties excited by an inverter having a dead time of 0 ns.

2 Experimental Method

Figure 1 shows a schematic illustration of the ring core and PWM inverter system used to measure the iron losses and magnetic *B-H* loop properties. The ring core is made of non-oriented (NO) electrical steel sheets (35H300) and is excited by a single-phase GaN inverter[13]. Note that GaN-FETs have the advantage of high-speed switching. The ratio of the amplitude of the fundamental sinusoidal waveform (at fundamental frequency f_0) to that of the triangular carrier waveform (at the carrier frequency f_c) is defined as the modulation index m. In our study, f_0 and m are set to 50 Hz and 0.7, respectively. We varied f_c from 400 kHz to 1.2 MHz in the steps of 200 kHz. The maximum magnetic flux density B_{max} of the ring core is set to 1.0 T and the dead time D is 0 ns.

The magnetic field intensity H and the magnetic flux density

B are derived, respectively, from the primary current I flowing through the primary winding and from the secondary voltage V induced in the secondary winding of the ring specimen. The iron loss W_{fe} is derived from H and B. Here, H, B, and W_{fe} are given by the following equations[13,14,17]:

$$B = \frac{1}{N_2 S}\int V\mathrm{d}t, \tag{1}$$

$$H = \frac{N_1 I}{l}, \tag{2}$$

$$W_{fe} = \frac{f_0}{\phi}\int H\mathrm{d}B, \tag{3}$$

where N_2 (= 10) denotes the number of turns of the secondary coil, S (= 87.5 mm^2) is the cross-sectional area of the ring core, N_1 (= 10) is the number of turns of the primary coil, l (= 0.36 m) is the magnetic path length of the core, and ϕ (= 7650 kg/m^3) is the density of the NO sheet.

In our study, the ratio η of the rise time T_{turnon} of the waveform to the on-time $T_{pulseon}$ of the pulse-voltage waveform of the PWM signal is defined to be

$$\eta = \frac{T_{turnon}}{T_{pulseon}}. \tag{4}$$

In this study, we derived η from the voltage waveform corresponding to the waveform of the minor loop closest to B = 0 T.

For our measurements, we used a voltage probe (Iwatsu Electric Co., Ltd., SS-320), a current probe (HIOKI E.E. Corp., CT6711), and a high-performance A/D converter (NI Corp., PXIe-5163, 14 bit, 1 GS/s).

3 Results and Discussion

We first discuss the magnetic B-H loop properties of the NO ring core under inverter excitation at high carrier frequencies and with D = 0 ns. The upper left and right panels in Fig. 2 (a), (b), and (c) show hysteresis loops at f_c = 400 kHz, 800 kHz, and 1.2 MHz, respectively. Due to the high harmonic components, the magnetic B-H loops contain numerous minor loops (see Refs.[4,11] for the minor loops). In a previous study[8], since ringing noise appeared, the investigators were unable to measure the minor loops clearly. Here, we found that the magnetic B-H loops include the minor loops of the magnetic materials even under inverter excitation at carrier frequencies on the order of MHz.

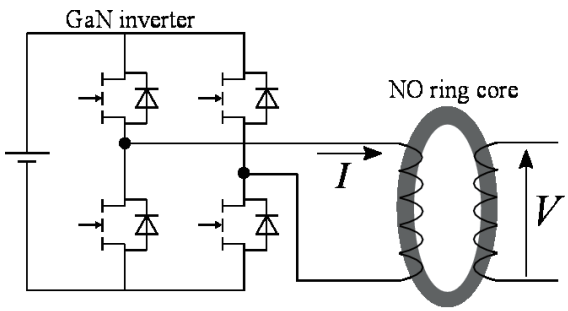

Fig. 1 Schematic illustration of the NO ring core and GaN inverter system used to measure the iron losses and magnetic B-H loop properties.

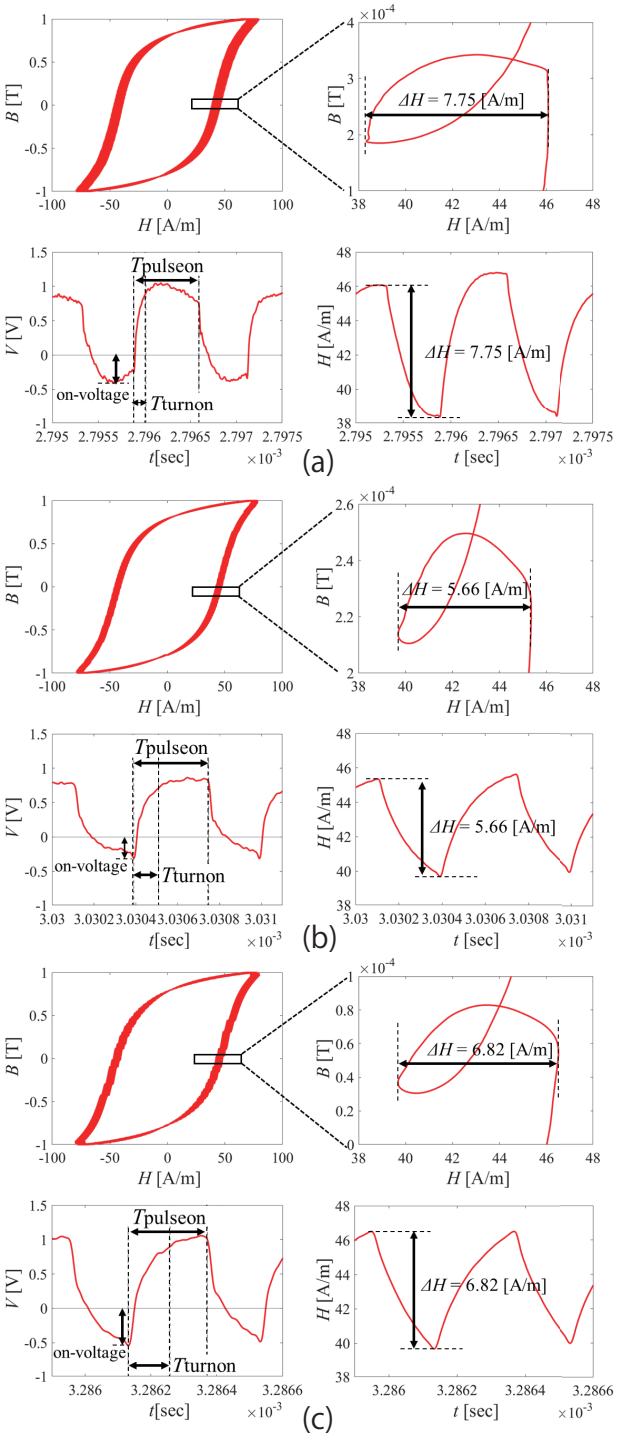

Fig. 2 Magnetic B-H loop (upper left panels), minor loop (enlarged view of part of the B-H loop, upper right panels), V waveform (lower left panels), and H waveform (lower right panels) of the NO ring core under inverter excitation at high carrier frequencies, with D = 0 ns. The width of the minor loop corresponds to the amplitude of the H waveforms. (a) 400 kHz. (b) 800 kHz. (c) 1.2 MHz.

The lower left panels in Fig. 2 show the waveforms of the secondary voltage V induced in the secondary winding of the NO ring specimen under GaN-FET inverter excitation. As shown in the figure, the on-voltage in V appears because GaN-FETs have on-resistance (see Refs.[11,13] for the on-voltage and the on-resistance.). In the high-frequency region (at 1.2 MHz), the ratio η of the rise time T_{turnon} of the waveform to the on-time T_{pulseon} [calculated from Eq. (4)] becomes large compared to that at 400 kHz.

Figure 3 shows the ratio η obtained from Eq. (4) as a function of the carrier frequency. As shown in this figure, η increases drastically with increasing carrier frequency. In other words, when the carrier frequency increases, the distortion of the pulse waveform becomes large, as shown in Fig. 4. When the waveform distortion increases, it is necessary to increase the voltage amplitude (pulse height), as shown in Fig. 4, to obtain the same magnetic flux density.

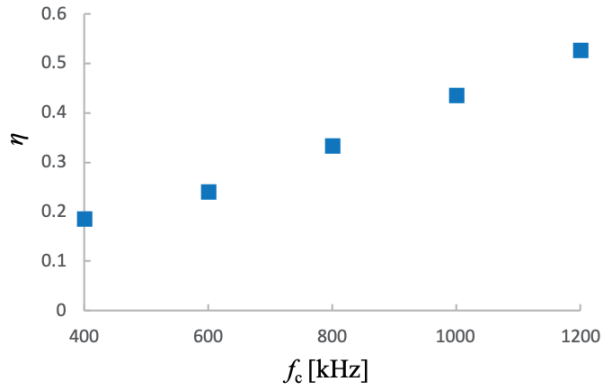

Fig. 3 The parameter η generated from Eq. (4) as a function of carrier frequency at D = 0 ns.

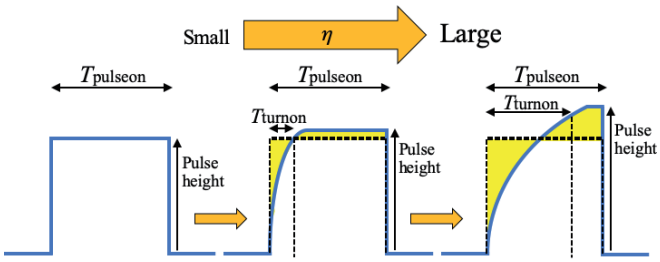

Fig. 4 Schematic illustration of the effects of waveform distortion on pulse height (amplitude of V). The areas highlighted in yellow above and below the flat top of each square pulse are equal.

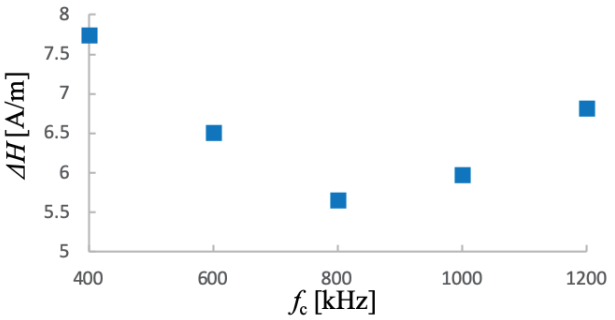

Fig. 5 The width ΔH as a function of carrier frequency at D = 0 ns.

Figure 5 shows the carrier-frequency dependence of the variation in the width ΔH in H by the time-harmonic components. In this study, we defined ΔH to be the variation in the width of H closest to B = 0 T, as shown in Fig. 2 (upper and lower right panels). The width ΔH first decreases and then increases as the carrier frequency increases. The decrease in ΔH in the NO ring under GaN-FET inverter excitation as the carrier frequency increases up to about 800 kHz is due to the skin effect[9,13]. At high carrier frequencies (more than about 800 kHz), ΔH increases again because the waveform distortion increases, as shown in Figs. 2 and 4, increasing the average amplitude of V.

Figure 6 shows the carrier-frequency dependence of the iron losses in the NO ring core fed by the PWM inverter at D = 0 ns. For comparison, the red line shows the iron losses under sinusoidal excitation. The iron losses in the NO ring core fed by the PWM inverter decrease in tandem with the increase in carrier frequency up to about 800 kHz and then increase. In the low-frequency region (less than about 800 kHz), the iron losses decrease due to the skin effect[9,13]. In the high-frequency region (above about 800 kHz), the iron losses increase again, because the distortion of the V waveform becomes larger, and ΔH increases, as shown in Figs. 2, 3, 4 and 5. Previous studies have shown that iron losses increase at high carrier frequencies due to the effects of dead time and ringing noise[7,8,17]. Our study shows for the first time that the iron losses also increase at high carrier frequencies due to the distortion of V. In other words, at high carrier frequencies, not only do the dead time and ringing noise cause increasing iron losses but also does the waveform distortion. Thus, to reduce the iron losses in a motor system under inverter excitation at high carrier frequencies, it is important to use a switching device that has a fast-rising waveform (high-

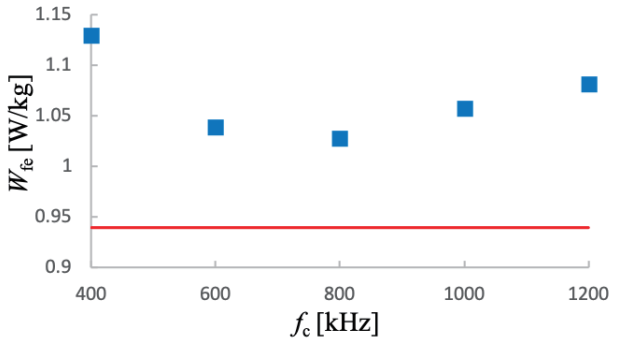

Fig. 6 Carrier-frequency dependence of the iron losses in the NO ring core fed by a PWM inverter at D = 0 ns. The solid blue squares show the losses under excitation by the inverter, and the red line shows those under sinusoidal excitation.

speed switching) and to apply an ideal pulse waveform with little distortion to the magnetic cores.

4 Conclusions

We have studied experimentally the iron losses and magnetic *B-H* loop properties of magnetic materials under PWM inverter excitation at high carrier frequencies on the order of MHz. We found that the magnetic *B-H* loops include minor loops due to the magnetic materials even at such high carrier frequencies. Our study showed for the first time that the iron losses increase at high carrier frequencies due to the distortion of *V*. These results open the way to further research on the reduction of iron losses under inverter excitation with high carrier frequencies by using high-speed switching and by applying an ideal pulse waveform with little distortion to the magnetic cores. In the future, we plan to use numerical simulations to evaluate quantitatively the impact of waveform distortions on iron losses.

Acknowledgments This work was partly supported by the JSPS KAKENHI ♯18K13749, ♯20K14721, JST OPERA ♯JPMJOP1841, JFE 21st Century Foundation, Kansai Research Foundation, Takeuchi Foundation, Nagamori Foundation Research Grant, and Sanken Electric Corporation.

References

1) A. Boglietti, P. Ferraris, M. Lazzari, and F. Profumo: *IEEE Trans. Magn.*, **27**, 5334 (1991).
2) A. Boglietti, P. Ferraris, M. Lazzari, and M. Pastorelli: *IEEE Trans. Magn.*, **31**, 4250 (1995).
3) A. Boglietti, P. Ferraris, M. Lazzari, and M. Pastorelli: *IEEE Trans. Magn.*, **32**, 4884 (1996)
4) M. Kawabe, T. Nomiyama, A. Shiozaki, H. Kaihara, N. Takahashi, and M. Nakano: *IEEE Trans. Magn.*, **48**, 3458 (2012).
5) K. Fujisaki and S. Liu: *J. Appl. Phys.*, **115**, 17A321 (2014).
6) T. Taitoda, Y. Takahashi, and K. Fujiwara: *IEEE Trans. Magn.*, **51**, 1 (2015)
7) T. Tanaka, S. Koga, R. Kogi, S. Odawara, and K. Fujisaki: *IEEJ J. Ind. Appl.*, **136**, 110 (2016) (in Japanese).
8) W. Martinez, S. Odawara, and K. Fujisaki: *IEEE Trans. Magn.*, **53**, 1 (2017).
9) A. Yao, K. Tsukada, S. Odawara, K. Fujisaki, Y. Shindo, N. Yoshikawa, and T. Yoshitake: *AIP Adv.*, **7**, 056618 (2017).
10) A. Yao, T. Sugimoto, S. Odawara, and K. Fujisaki: *AIP Adv.*, **8**, 056804 (2018).
11) A. Yao, S. Odawara, and K. Fujisaki: *IEEJ J. Ind. Appl.*, **7**, 298 (2018).
12) A. Yao, T. Sugimoto, S. Odawara, and K. Fujisaki: *IEEE Trans. Magn.*, **54**, 1 (2018).
13) A. Yao, K. Tsukada, and K. Fujisaki: *IEEJ J. Ind. Appl.*, **7**, 321 (2018).
14) A. Yao, T. Sugimoto, and K. Fujisaki: *IEEJ J. Ind. Appl.*, **139**, 276 (2019) (in Japanese).
15) A. Yao, T. Sugimoto, and K. Fujisaki: *J. Magn. Soc. Jpn.*, **43**, 42 (2019).
16) A. Yao and T. Hatakeyama: *J. Magn. Soc. Jpn.*, **43**, 46 (2019).
17) A. Yao, T. Funaki, and T. Hatakeyama: *J. Magn. Soc. Jpn.*, **43**, 105 (2019).
18) A. Yao: *J. Magn. Soc. Jpn.*, **44**, 52 (2020).
19) A. Yao, R. Moriyama, and T. Hatakeyama: *J. Magn. Soc. Jpn.*, (2020) doi: 10.3379/msjmag.2005L001.

Recieved Feb. 26, 2020; Accepted Apr. 30, 2020

J. Magn. Soc. Jpn., **44**, 91-95 (2020)

<Paper>

Flux growth and magnetic properties of single crystals of hexagonal ferrite structures and a long-range-order structure

T. Saho, T. Fujihara, K. Kakizaki, and K. Kamishima

Graduate School of Science and Engineering, Saitama University, *255 Shimo-Okubo, Saitama 338-0825, Japan*

We prepared single crystals of six typical hexaferrites (M-type, W-type, X-type, Y-type, Z-type, and U-type) in order to investigate their formation, crystal size, and magnetic properties. In addition, we also investigated the conditions of single-crystal formation at several flux concentrations and cooling rates. We found that the growth of single crystals on the MY-line (Y- and Z-type) became more significant than that on the MS-line (W-type) under a slow-cooling condition. In contrast, the single crystals on the MS-line appeared with a relatively high cooling rate of 10°C/h., where the single crystals did not grow large. By using the self-flux method, we succeeded in synthesizing single crystals with a more complex structure with a possibility of being M_2Y_7 on the MY-line and investigating the magnetic properties.

Key words: hexagonal ferrite, flux method, long-range-order, single crystal

1. Introduction

Due to their spontaneous magnetization at room temperature, low electrical conductivity, and high corrosion resistivity, ferrites occupy a critical role in a wide range of technological applications. The most popular classes of ferrites are the cubic spinels, garnets, and hexagonal magnetoplumbites (M-type hexaferrite). Hexaferrites play an important role in permanent magnet and microwave absorber applications owing to their uniaxial or in-plane anisotropy depending on their crystal structures with a wide variety.[1)]

There are three stacking units for hexaferrites; a spinel-like S-block ($(2MeFe_2O_4)^{0\pm}$, $(2Fe_3O_4)^{2+}$), an R-block ($(BaFe_6O_{11})^{2-}$), and a T-block ($(Ba_2Fe_8O_{14})^{0\pm}$) as shown in Fig. 1. Combinations of T-, S-, and R-blocks in Fig.2 yield the magnetoplumbite M-type $BaFe_{12}O_{19}$ (RSR*S*), W-type $BaMe_2Fe_{16}O_{27}$ ($RS_2R^*S^*_2$), X-type $Ba_2Me_2Fe_{28}O_{46}$ ($[RS_2R^*S^*]_3$) structures, Y-type $Ba_2Me_2Fe_{12}O_{22}$ ($[TS]_3$), Z-type $Ba_3Me_2Fe_{24}O_{41}$ (RSTSR*S*T*S*), and U-type $Ba_4Me_2Fe_{36}O_{60}$ ($[RSTSR^*S^*]_3$) structures, where Me is a divalent transition metal cation and the block with an asterisk is turned 180° around the c-axis.[2-3)] Also, Kohn *et al*. suggested the existence of more complicated structures between the M-type and X-type hexaferrites and between the M-type and Y-type hexaferrites.[3-8)]

Although some research has been carried out on the magnetic properties of a single crystal of a specific hexaferrite, no single study exists about which condition is preferable for the hexaferrite single crystal to grow. Few studies assessed several conditions to grow single crystals, but it seems that the conditions of mixing ratios of raw materials, heating temperatures, and duration periods were randomly selected. [4, 9, 10)] The complicated structures were also based upon just the description of the stacking arrangements of S-, T-, and R-blocks with no crystallographic evidence. [4-8)]

In this study, the hexaferrite single crystals were prepared by the use of flux growth. The main advantage of the flux method is that crystal growth takes place at a temperature lower than that required by the pure melt for growth. A lower synthesis temperature enables us to avoid the decomposition of the target material before melting and the divergence from an initial composition due to volatility.

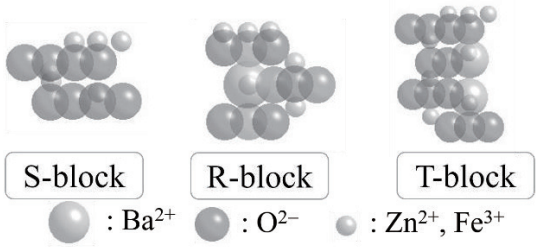

Fig. 1 Three basic blocks as part of crystal structures of hexaferrites.

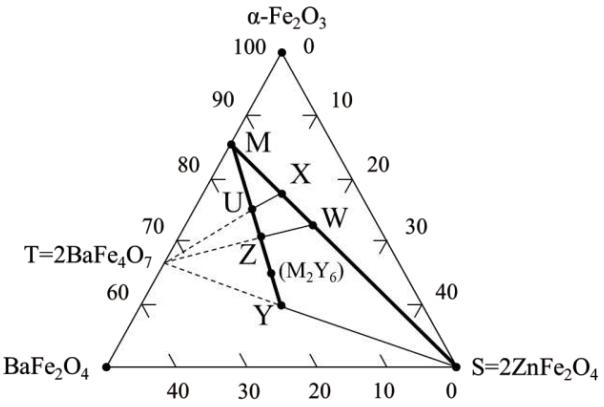

Fig. 2 Six typical hexaferrites in a partial diagram of the α-Fe_2O_3-BaO-ZnO system.

The main purpose of this study is to develop an understanding of the conditions where single crystals of the desired hexaferrite grow. This paper also demonstrates the usefulness of the single-crystal-growth conditions by synthesizing a single crystal with a complicated block-stacking structure.

2. Experimental

Samples were prepared by the self-flux method with an appropriate flux, BaB_2O_4 (T_m=1105°C). We used $BaCO_3$, ZnO, α-Fe_2O_3, and B_2O_3 as starting materials. Single crystals of several hexagonal ferrites were grown at ratios of BaO : ZnO : α-Fe_2O_3 =

1 : 2 : 8 (W-type), 1 : 1 : 3 (Y-type), 3 : 2 : 12 (Z-type), and others. The flux was weighed to three molar ratios (25, 50, 75 mol%) to the desired hexaferrite. These mixtures in platinum crucibles were kept at 1200~1300°C for five hours and then cooled at a rate of 2~10°C/h to 1050°C. Finally, they were cooled down to room temperature. The crystals were separated from the melt by the use of nitric acid or hydrochloric acid for a few weeks at room temperature. The crystals were classified into three groups by size (> 1 mm, 1~0.3 mm, < 0.3 mm).

To investigate the structure, composition, and properties of the samples, they were examined by the following methods. X-ray diffraction analysis (XRD) with Cu-Kα radiation was performed to characterize the crystalline structure. The chemical compositions of the grown samples were estimated by the use of an electron scanning microscope (SEM) with an energy dispersive X-ray spectrometer (EDX) for elemental analysis. Magnetization was measured by using a vibrating sample magnetometer (VSM) and a superconducting quantum interference device (SQUID) magnetometer.

3. Results and discussions

3.1 Growth of known-structure single crystals

Before synthesizing single crystals of long-range-order hexaferrites, we have prepared single crystals of six typical hexaferrites (M-type, W-type, X-type, Y-type, Z-type, and U-type) in order to investigate their formation, crystal size, and magnetic properties. The preparation conditions were as follows. The initial compositions were BaO : ZnO : α-Fe_2O_3 = 1 : 0 : 6 (M-type), 1 : 2 : 8 (W-type), 2 : 2 : 14 (X-type), 1 : 1 : 3 (Y-type), 3 : 2 : 12 (Z-type), 4 : 2 : 18 (U-type). The cooling rate was 10°C/h., and three kinds of solvent molar ratios were used at 25, 50, and 75 mol%.

Figure 3 shows the XRD patterns of the powder samples to which single crystals of the typical hexaferrites were ground. The XRD patterns of the M-type, W-type, Y-type, Z-type, and U-type samples demonstrated the corresponding single phases. On the other hand, the other XRD pattern of the X-type ferrite sample suggested contamination with tiny crystals of M-type hexaferrite.

Figure 4 shows the thermal magnetization curves of these six kinds of hexaferrites. The Curie temperatures of the M-type and Y-type ferrite samples corresponded to those in Ref. 1. The Curie temperature of the W-type sample was in agreement with that of a single crystal prepared by another flux method.[4] The Curie temperature of the Z-type sample was just between those of M-type and Y-type ferrite samples, which possibly comes from the intermediate crystal structure of the Z-type ferrite between the M-type and Y-type ferrite structures. The Curie temperatures of X-type and U-type ferrite samples were between those of the M-type and W-type samples, and between those of the M-type and Z-type samples, respectively. The former Curie temperature reflects the intermediate X-type structure between the M-type and W-type ones, and the latter reflects the intermediate U-type between the M-type and Z-type, respectively. The temperature dependence of magnetization of the X-type sample shows two Curie temperatures, being consistent with the corresponding XRD result of the M-type and X-type mixed phases.

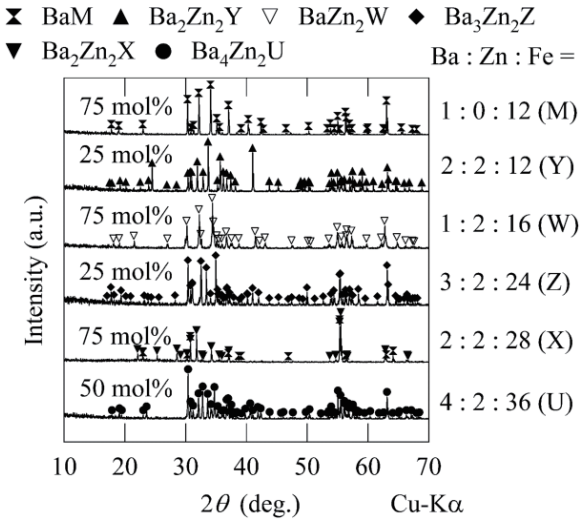

Fig. 3 XRD patterns of M-, W-, X-, Y-, Z-, and U-type hexaferrites.

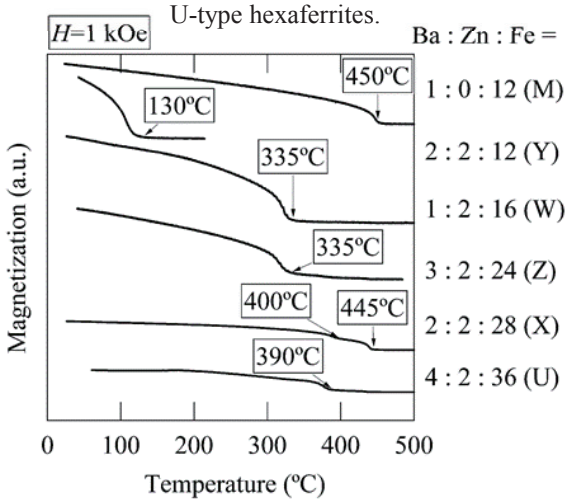

Fig. 4 Thermal magnetization curves of M-, W-, X-, Y-, Z-, and U-type hexaferrites.

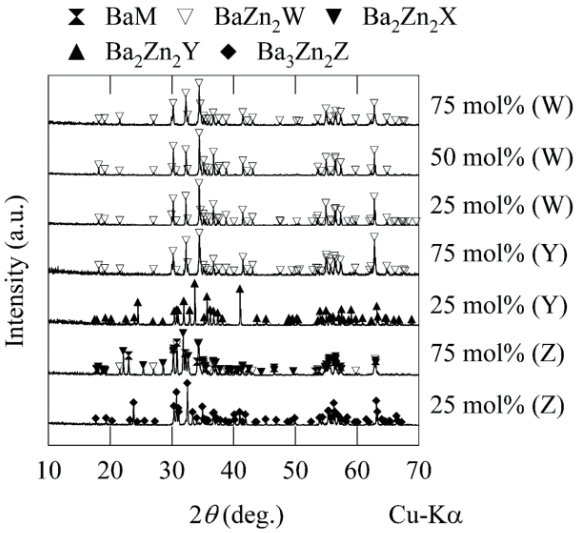

Fig. 5 XRD patterns of W-type, Y-type, and Z-type composition samples prepared in three molar ratios (75, 50, 25 mol%).

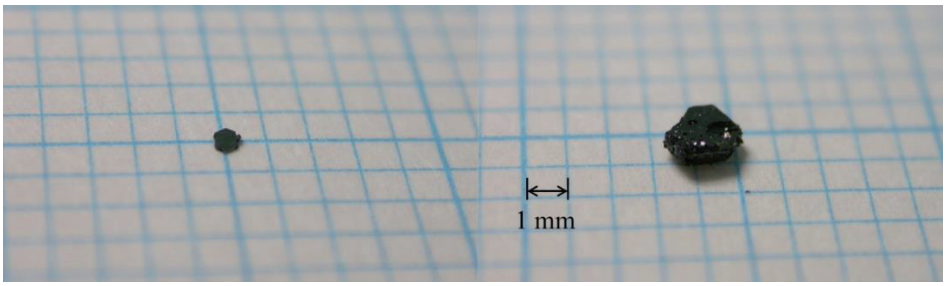

Fig. 6 Photographs of
(a) M-type and (b) Y-type ferrite single crystals.

Although the X-type hexaferrite between the M-type and W-type was accompanied by the M-type hexaferrite, we succeeded in synthesizing six known hexaferrites. Having found that six known hexaferrites can be synthesized under the same condition, we also investigated the different conditions of single-crystal formation in the next section.

3.2 Solubility of samples with compositions on the MS-line and MY-line

We also investigated the conditions of single-crystal formation, focusing on the molar concentration of the flux. The preparation conditions of the single crystals in this section were the same as those in the previous section. Figure 5 shows the XRD patterns of the W-type, Y-type, and Z-type composition powder samples, to which the single crystals were ground. These three kinds of preparation compositions resulted in a striking difference in the formation of crystallographic phases, which depended on the three molar ratios. All the XRD patterns of the W-type samples demonstrated the corresponding single phase, and the single crystal size became larger as the flux molar ratio was increased. On the other hand, the XRD patterns of the Y-type and Z-type samples were accompanied by the diffraction peaks of other hexaferrites, and the sizes of these single crystals were also different. The Y-type and Z-type composition samples with the largest-molar-ratio flux (75 mol%) contained the M-type, W-type, and X-type phases located on the MS-line in the BaO-ZnO-Fe_2O_3 phase diagram, and those with the flux ratio of 50 mol% also included the W-type phase. The samples with the flux ratio of 25 mol% only showed the desired Y-type and Z-type patterns, respectively. Although these results should be treated as part of a quaternary diagram of BaO-Fe_2O_3-ZnO-B_2O_3, to the best of our knowledge, the corresponding diagram is not available, which led us to the following alternative interpretation. These results are possibly due to the difference in solubility of the typical hexaferrite structures. Specifically, the hexaferrite structures on the MY-line seem to have a higher solubility than the structure of the MS-line. This higher solubility is consistent with the fact that an attempt to synthesize the T-block composition sample alone gives rise to the melt. Combining this high solubility with a relatively fast cooling rate of 10°C/h can prevent the single-crystal structures on the MY-line from growing from the solution. Therefore, the structure on the MS-line was easily formed in the Z-type-composition sample with the largest-molar-ratio flux (75 mol%), and the structure on the MY-line appeared at the flux ratios of 50 and 25 mol%.

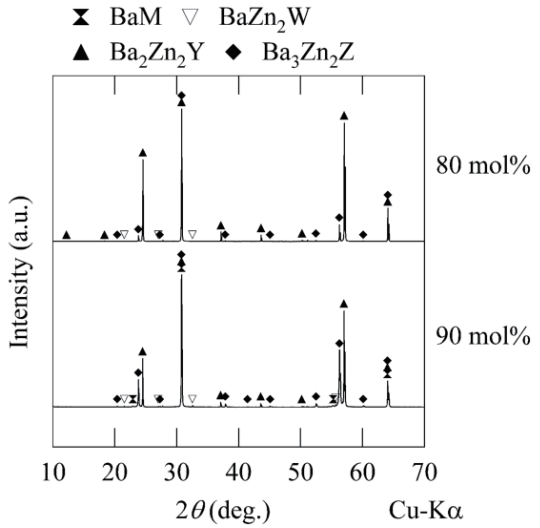

Fig. 7 XRD patterns of single crystals prepared at a slow-cooling rate of 4°C/h and higher molar ratios.

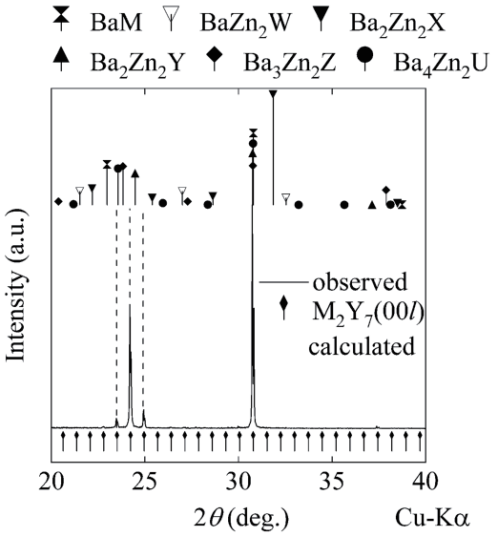

Fig. 8 XRD pattern of a single crystal with a long-range-order structure.

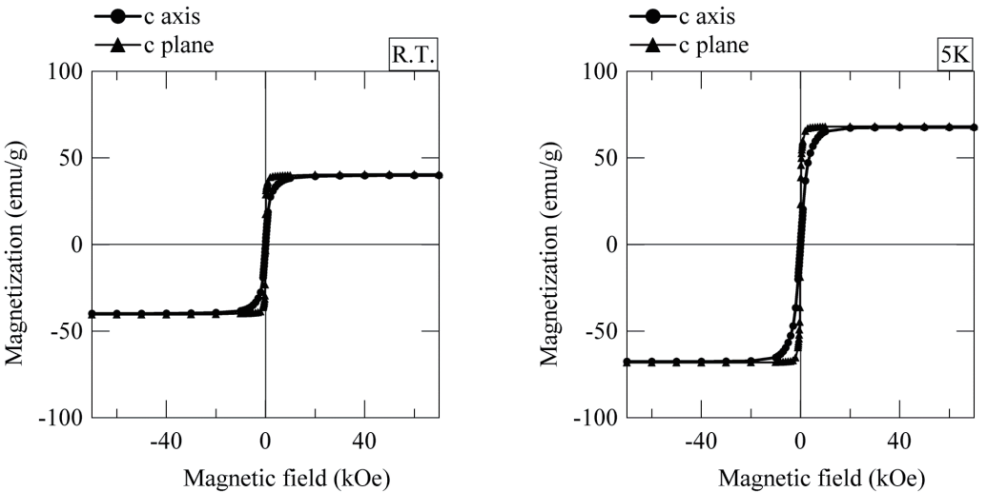

Fig. 9 Hysteresis loops of a single crystal with a long-range-order structure.

3.3 Crystal growth of samples on the MS-line and MY-line

This section describes the features of the crystal growth of hexaferrites. The size of a single crystal depended on the kind of hexaferrite. For example, the largest single crystal had a diameter of 2 mm for the Y-type ferrite, whereas that of the U-type hexaferrite was between 0.3 and 1.0 mm. Figures 6 (a) and (b) show photos of an M-type and a Y-type ferrite single crystal, respectively, which had the shape of a hexagonal plate. M-type ferrite samples were grown in the in-plane directions, whereas Y-type ferrite samples were in the *c*-axis. As a general tendency, the single crystals on the MY-line in Fig. 2 were grown more significantly than the single crystals on the MS-line.

3.4 Effect of a slow cooling rate and high molar ratios of solvent

We also attempted to obtain larger single crystals by adopting synthesis conditions with a slow cooling rate and high molar ratios of solvent. These single crystals were prepared at the initial composition of BaO : ZnO : α-Fe_2O_3 = 14 : 12 : 96 (2M + 6Y as marked in Fig. 2), the cooling rate of 4°C/h, and the solvent molar ratios of 90 and 80 mol%. Figure 7 shows the XRD patterns of several single crystals that were prepared with the conditions described above. Although various phases of hexaferrites were observed in these patterns, the majority phases were those on the MY-line. The initial composition was between the Z-type and the Y-type composition, and the flux ratios were higher than 75 mol%. Therefore, the formation of the single crystals on the MS-line like the W-type hexaferrite was expected, as in Fig. 5. However, the single crystals on the MY-line appeared more significant than those on the MS-line. This discrepancy suggests a characteristic in the growth of the single crystals on the MY-line. Here, it should be noted that the sizes of the single crystals on the MY-line were larger than those on the MS-line even in this slow-cooling condition. This slow cooling condition counteracted the high flux ratio that tends to prevent the first step of the formation of tiny crystals on the MY-line.

These results implied that the slow cooling helped the growth of the single crystals on the MY-line, which was easier than those on the MS-line. This finding motivated us to look for single crystals with a more complex structure on the MY-line. We investigated the other single crystals collected from the sample batch prepared with the slow cooling condition in this section in more detail, because the batch possibly contained a single crystal with a more complex structure on the MY-line, as shown in the next section.

3.5 The long-range-order hexaferrite

We found a single crystal with a long-range-order structure from the sample batch in the same crucible used in the previous section. The composition analysis of this single crystal showed Ba : Zn : Fe = 16.00 : 13.98 : 121.8, which was consistent with the M_2Y_7 composition. This composition was close to the initial composition of 2M + 6Y, to which the self-flux method contributed as an advantage. Figure 8 shows the XRD pattern of the discovered single crystal possibly having the M_2Y_7 structure. The vertical lines in Fig. 8 represent the (00*l*) peaks calculated from the M_2Y_7 structure with *c*=249.7 Å derived from a Y-unit (TS) thickness of 14.5 Å and an M-unit (RS) thickness of 11.6 Å. [2] This unit cell consists of two chemical formulae ($2M_2Y_7$), where the upper-half part of the unit cell is turned 180° around the c-axis compared with the lower-half part of the unit cell, giving rise to (00*l*) reflections where *l* is an even integer. Considering other possibilities of various combinations of M and Y units, [5] we found the M_2Y_7 combination to generate (00*l*) peaks in agreement with the significant peaks around 24° and 31° and the other small peaks in Fig. 8. These calculated (00*l*) peaks explain the observed experimental peaks well, but the diffraction peaks of the typical hexaferrites are inconsistent with them. This fact strongly suggests the crystal growth of the complex M_2Y_7 structure. The hysteresis loops of this single crystal were measured at 300 and 5 K, as shown in Figs. 9 (a) and (b), respectively. These hysteresis loops clearly show that the sample is ferromagnetic at 300 and 5 K. The saturation magnetization at 5 K is in the range of 70~90 emu/g due to an error in the mass estimation of the M_2Y_7 tiny crystal. On the other hand, assuming that one M unit has 20 μ_B and one Zn_2Y unit has 18.4 μ_B at low temperatures, [2] we can calculate the magnetization of one M_2Y_7 formula unit as 77 emu/g. This estimated value is within the error of the observed

magnetization.

To sum up, we succeeded in synthesizing the complex structure with a possibility of being M_2Y_7 and investigating the magnetic properties.

4. Conclusion

We found that the growth of single crystals on the MY-line became more significant than that on the MS-line in the slow-cooling condition.

In contrast, the single crystals on the MS-line appeared with a relatively high cooling rate of 10°C/h where the single crystals did not grow large, as shown in section 3.2.

These results suggest the difference between the MS-line and the MY-line structures in the nucleation and the crystal growth speed. The nuclei of the hexaferrites on the MS-line can be formed easier than those on the MY-line at first. On the other hand, the difference in the growth speed enabled the MY-line composition crystals to become the majority phases of single crystals.

By using these properties in the self-flux method, we succeeded in controlling the growth of the single crystals and obtaining the single crystal of a complex structure with a possibility of being M_2Y_7. Further work needs to be done to determine the exact block-stacking combination with atomic coordinates from this possibility of M_2Y_7 structure.

References

1) M. Sugimoto: *J. Am. Ceram. Soc.*, **82**, 269 (1999).
2) J. Smit and H. P. J. Wijn: Ferrites, pp. 177-211 (Philips Technical Library,1959).
3) P. B. Braun: *Philips Res. Rep.*, **12**, 491 (1957).
4) R. O. Savage and A. Tauber: *J. Am. Ceram. Soc.*, **47**, 13 (1964).
5) J. A. Kohn, D. W. Eckart, C. F. Cook, and Jr.: *Science*, **172**, 519 (1971).
6) J. A. Kohn and D. W. Eckart: *Z. Kristallogr*, **119**, 454 (1964).
7) J. A. Kohn and D. W. Eckart: *Z. Kristallogr*, **124**, 69 (1967).
8) J. A. Kohn and D. W. Eckart: *Z. Kristallogr*, **125**, 130 (1967).
9) D. A. Vinnik, A. Y. Tarasova, D. A. Zherebtsov, S. A. Gudkova, D. M. Galimov, V. E. Zhivulin, E. A. Trofimov, S. Nemrava, N. S. Perov, L. I. Isaenko, and R. Niewa: *Materials (Basel).* **10** (6), 578 (2017).
10) T. S. Chin., S. L. Hsu, and M. C. Deng: *J. Magn. Magn. Mat.*, **120**, 64 (1993).

Received Feb. 06, 2020; Revised Mar. 16, 2020; Accepted Apr. 7, 2020

J. Magn. Soc. Jpn., **44**, 96-101 (2020)

<Paper>

Robustness and Local Polarization Control of Plasmonic Antennas with Fabrication Errors

Ryohei Ohnishi*, Keisuke Tatsuzawa*, Takashi Yamaguchi**, Seiya Kishimoto*, Yoshito Ashizawa*, Katsuji Nakagawa*, and Shinichiro Ohnuki*

*Nihon University, *8-14, Kanda-surugadai 1-chome, Chiyoda-ku, Tokyo 101-8308, Japan*

**Tokyo Metropolitan Industrial Technology Research Institute, *2-4-10, Aomi, Koto-ku, Tokyo 135-0064, Japan*

All-optical magnetic recording with circularly polarized light has attracted attention for ultra-high-speed magnetic recording. To obtain high-density magnetic recording, localized light over the diffraction limit is required. Nanoantennas have been designed to generate localized circularly polarized light for high-density all-optical magnetic recording system. The amplitude and phase of the localized light depend on the incident wavelength, shapes, and materials of antennas. To realize these practical systems, the antenna shape must be robust against fabrication errors. Therefore, we propose an antenna shape with high robustness against these errors. Furthermore, a control method for the amplitude and phase of localized light is proposed.

Keywords: all-optical magnetic recording, circularly polarized light, nano-antennas, plasmonic antenna

1. Introduction

Recently, recording speeds achieved using conventional magnetic recordings have reached a theoretical limit. All-optical magnetic recording with circularly polarized light is an ultra-fast magnetic recording system that can be 100,000 times faster than the conventional system [1)-5)]. To obtain high-density magnetic recording, localized light over the diffraction limit is required.

The performance of plasmonic antennas has been studied because antennas can localize circularly polarized light beyond the diffraction limit[6)-11)]. The amplitude and phase of localized light depend on the incident wavelength, shapes, and materials of antennas. Antennas can be designed via recent fabrication techniques. However, fabrication errors occur in such antennas, thereby affecting the generation of circularly polarized light.

The stabilization of high-density and high-speed magnetic recording is also discussed. Robustness for the generation of circularly polarized light is investigated with varying antenna shapes. The control method for the amplitude and phase of localized light is studied using plasmonic antennas. The proposed method can be applied to control the polarization of localized light generated by arbitrary antenna shapes. Furthermore, the proposed system is verified using plasmonic antennas for an ultra-fast magnetic recording system.

2. Formulation

2.1 ADE–FDTD method

To design and evaluate plasmonic antennas, the finite-difference time-domain (FDTD) method combined with the auxiliary differential equation (ADE) method is applied [12-13)]. Coupled Maxwell's equations and the following motion equation for l-th electron are considered to simulate the near-field light generated by plasmonic antennas [12)]:

$$m\frac{d^2\mathbf{u}_l}{dt^2}+m\nu_l\frac{d\mathbf{u}_l}{dt}+m\omega_l^2\mathbf{u}_l=q\mathbf{E}, \tag{1}$$

where m is effective mass of electron, $\mathbf{u}_l$ is displacement vector, t is time, ν_l is collision frequency, ω_l is resonance frequency, q is charge, and $\mathbf{E}$ is the electric field. The motion equation of electron is considered to express the polarization current inside dispersive media.

The electromagnetic fields can be calculated using the finite-difference scheme for the coupled equations. The finite-difference forms of the electric and magnetic fields, polarization, and current can be expressed as follows [12,13)]:

$$\mathbf{E}^{n+1}=C_1\mathbf{E}^n+C_2\left[\nabla\times\mathbf{H}^{n+1/2}-\frac{1}{2}\sum_{l=0}^{K}\{(1+\alpha_l)\mathbf{J}_l^n-\gamma_l\mathbf{P}_l^n\}\right] \tag{2}$$

$$\mathbf{H}^{n+1/2}=\mathbf{H}^{n-1/2}-\frac{\Delta t}{\mu_0}\nabla\times\mathbf{E}^n \tag{3}$$

$$\mathbf{P}_l^{n+1}=\mathbf{P}_l^n+\frac{\Delta t}{2}\left(\mathbf{J}_l^{n+1}+\mathbf{J}_l^n\right) \tag{4}$$

$$\mathbf{J}_l^{n+1}=\alpha_l\mathbf{J}_l^n+\beta_l\left(\mathbf{E}_l^{n+1}+\mathbf{E}_l^n\right)-\gamma_l\mathbf{P}_l^n, \tag{5}$$

where, $\mathbf{H}$ is the magnetic field, $\mathbf{J}_l$ is current density vector, $\mathbf{P}_l$ is polarization vector, Δt is time step size,

$$\begin{cases} C_1=\dfrac{2\varepsilon_0-\Delta t\sum_{l=0}^{K}\beta_l}{2\varepsilon_0+\Delta t\sum_{l=0}^{K}\beta_l}, C_2=\dfrac{2\Delta t}{2\varepsilon_0+\Delta t\sum_{l=0}^{K}\beta_l} \\ \alpha_l=\dfrac{1}{\xi_l}\left\{1-\dfrac{\Delta t}{4}(2\nu_l+\omega_l^2\Delta t)\right\} \\ \beta_l=\dfrac{\varepsilon_0 A_l\omega_p^2\Delta t}{2\xi_l}, \gamma_l=\dfrac{\omega_l^2\Delta t}{\xi_l}, \\ \xi_l=1+\dfrac{\Delta t}{4}(2\nu_l+\omega_l^2\Delta t) \end{cases} \tag{6}$$

ε_0 is permittivity for vacuum, and A_l is coefficients for Lorentz-Drude model.

Using the computed values of the electric field, the circularity C' of the localized light is defined[15), 16)] as follows:

$$C'=\frac{2\langle E_x(t)E_y(t)\sin(\delta_x(t)-\delta_y(t))\rangle}{\langle E_x^2(t)\rangle+\langle E_y^2(t)\rangle+\langle E_z^2(t)\rangle}, \tag{7}$$

where $E_x(t)$, $E_y(t)$, and $E_z(t)$ are the amplitude of each

electric field component, $\delta_i(t)$ is the phase of i component of the electric field, and $(\delta_x(t) - \delta_y(t))$ is the phase difference between x and y components of the electric field. This definition has been slightly modified to consider the normal component $E_z(t)$ in the denominator.

2.2 Computational model

Figure 1 shows the computational model of a plasmonic antenna. The size of the antenna is mainly characterized by the *X-length*, *Y-length*, and *Z-thickness*. The antenna is composed of metal characterized by the dispersion model. The size of the antenna is selected to generate a 90° phase difference between the electric x and y components. This is the condition to obtain the localized circularly polarized light ideal for realizing the ultra-fast magnetic recording system[1]. The blue dots are assumed to be particulate recording media. These particles are placed to achieve the recording density over a few Tbits/in^2. The proposed antenna is optimized to generate circularly polarized light at the center of the particulate recording medium. Figure 2(a) shows the Lissajous plot of the electric field component in the particulate recording media. The circularly polarized light is generated with time. If the optimized antenna has fabrication errors, elliptical polarization is generated as shown in Figure 2(b).

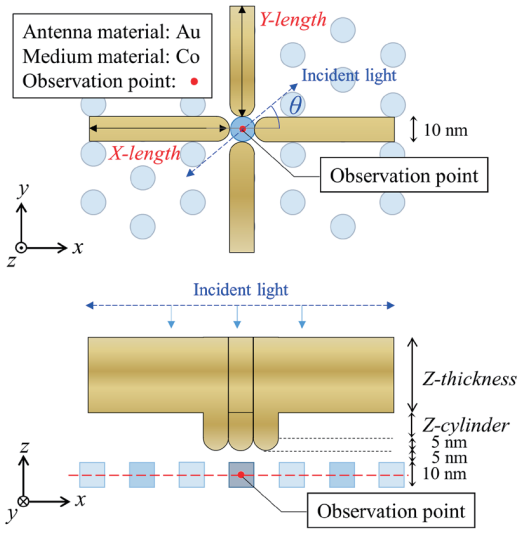

Fig. 1 Computational model of plasmonic antennas with particulate recording media. Circularly polarized light is generated at center of particulate recording medium.

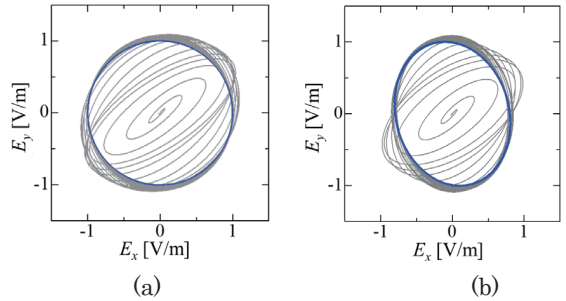

Fig. 2 Lissajous plot of electric field components in particulate recording media. (a) Optimized plasmonic antenna.(b) Plasmonic antenna with fabrication errors.

2.3 Control for the polarization of localized light

The incident light is assumed to be a sinusoidal plane wave that propagates in the negative z direction. Using a plasmonic antenna, we propose a method to localize and generate circularly polarized light inside the target medium, below and at the center of the antenna. Figure 3 shows a simple procedure to study the polarization of localized light generated by the plasmonic antenna. Similar to incident light, we assume that the following circularly polarized light impinges:

$$\begin{pmatrix} E_x \\ E_y \end{pmatrix} = \begin{pmatrix} \kappa\cos(\omega t) \\ -\kappa\sin(\omega t) \end{pmatrix} \tag{8}$$

where κ is the amplitude of circularly polarized light.

Typically, light generated by an arbitrary shape of plasmonic antennas is elliptically polarized owing to the difference in amplitude and phase between the x and y electric components. The characteristic of elliptical polarization is indicated by three parameters: α and β correspond to the major and minor axes, respectively. γ is the rotational angle of the x component. Therefore, the polarization of this antenna system is represented by the matrix form, such as

$$\begin{pmatrix} \cos\gamma & -\sin\gamma \\ \sin\gamma & \cos\gamma \end{pmatrix} \begin{pmatrix} \alpha & 0 \\ 0 & \beta \end{pmatrix}. \tag{9}$$

Figure 4 summarizes how circular polarization is obtained inside the target medium. When we design the polarization as shown in Figure 4(a), the incident light can be expressed by

$$\begin{pmatrix} E_x \\ E_y \end{pmatrix} = \begin{pmatrix} \cos\gamma & -\sin\gamma \\ \sin\gamma & \cos\gamma \end{pmatrix} \begin{pmatrix} \beta & 0 \\ 0 & \alpha \end{pmatrix} \begin{pmatrix} \kappa\cos(\omega t) \\ -\kappa\sin(\omega t) \end{pmatrix}. \tag{10}$$

Considering the field enhancement and phase delay of the antenna system, the x and y components of localized light are expressed as

$$\begin{pmatrix} E_x \\ E_y \end{pmatrix} = \begin{pmatrix} \cos 2\gamma & -\sin 2\gamma \\ \sin 2\gamma & \cos 2\gamma \end{pmatrix} \begin{pmatrix} \alpha\beta & 0 \\ 0 & \alpha\beta \end{pmatrix} \begin{pmatrix} \kappa\cos(\omega t) \\ -\kappa\sin(\omega t) \end{pmatrix}. \tag{11}$$

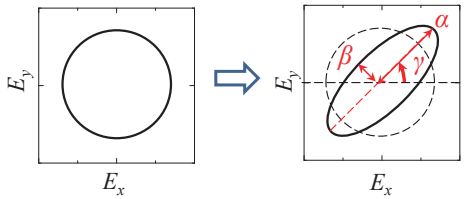

Fig. 3 Simple procedure for studying polarization of localized light generated by plasmonic antenna.

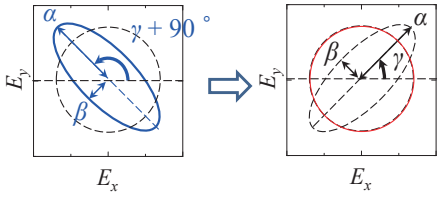

Fig. 4 Brief representation of the way to obtain circular polarization inside target medium.

Table 1 Size of optimized antenna for generating circularly polarized light.

Parameter	Pattern (a)	Pattern (b)	Pattern (c)
Z-thickness (nm)	15	30	60
Z-cylinder (nm)	10	10	10
X-length (nm)	70	84	99
Y-length (nm)	64	74	79
θ (°)	33.6	54.1	43.5
Circularity C'	1.0	1.0	1.0
Intensity I ((V/m)²)	0.744	1.108	1.826

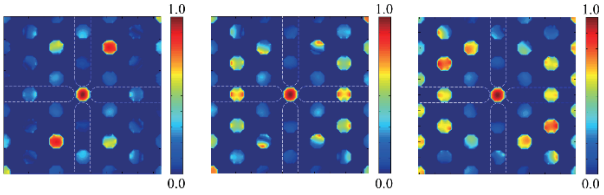

(a) (b) (c)

Fig. 5 Distribution of circularity C' on observation plane for patterns (a), (b), and (c).

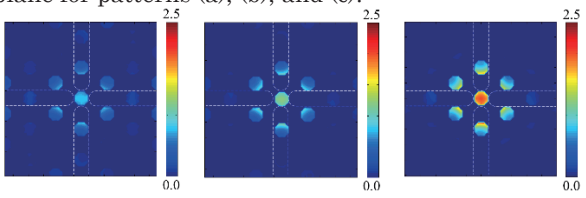

(a) (b) (c)

Fig. 6 Distribution of intensity I on observation plane for patterns (a), (b), and (c).

Table 2 Antenna size with fabrication errors. The *X-length* increases by 5 nm.

Parameter	Pattern (a')	Pattern (b')	Pattern (c')
Z-thickness (nm)	15	30	60
Z-cylinder (nm)	10	10	10
X-length (nm)	70+5	84+5	99+5
Y-length (nm)	64	74	79
θ (°)	33.6	54.1	43.5
Circularity C'	0.762	0.862	0.969
Intensity I ((V/m)²)	0.459	0.759	1.505

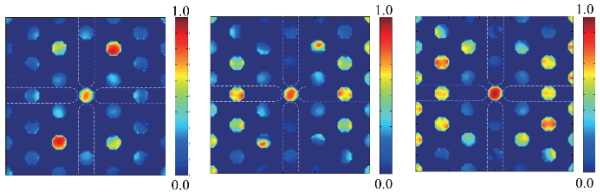

(a) (b) (c)

Fig. 7 Distribution of circularity C' on observation plane for patterns (a′), (b′), and (c′).

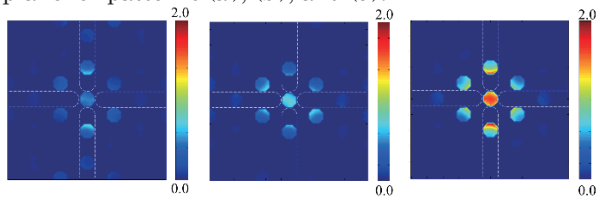

(a) (b) (c)

Fig. 8 Distribution of intensity I on observation plane for the patterns (a′), (b′), and (c′).

In Eq. (11), the light generated by any plasmonic antenna becomes circularly polarized through the proposed method.

3. Computational results

This section discusses the polarization of localized light generated by various plasmonic antennas. The original antenna shape was designed via simulation and the ideal circularly polarized light could be obtained[14]. In the following subsection, the antenna shape is slightly modified from the original one to consider sufficient margin for the nanofabrication process.

3.1 Investigation of robustness of antenna shape against fabrication error

The robustness of the circularity C' and intensity I was investigated for varying antenna shapes. Table 1 shows the optimized size of plasmonic antennas for generating circularly polarized light in particle recording media at the center of the antenna. Each pattern has a different antenna thickness, called *Z-thickness*. Figures 5 and 6 show the distribution of the circularity C' and intensity I on the observation plane, respectively. The circularly polarized light can be generated in particle recording media for all patterns. The maximum intensity I in particle recording media at the center of the antenna can be obtained from Figure 6.

We discuss the robustness of antenna shape against fabrication error in Table 2. The *X-length* increases by 5 nm from the original parameter for patterns (a), (b), and (c). The circularity C' in particle recording media at the center of the antenna are 0.762, 0.862, and 0.969 for Figures 7(a), 7(b), and 7(c), respectively. The intensity I increases with the *Z-thickness* as shown in Figure 8. The degradation of the circularity C' decreases and the intensity I increases, as the *Z-thickness* increases. Thus, high robustness toward shape change can be expected at a *Z-thickness* of 60 nm. The same characteristic is preserved for varying the *Y-length.*

The physical reason for the achieving robustness of large *Z-thickness* is clarified. The electric fields around plasmonic antennas for patterns (a), (b), and (c) are shown in Figure 9. The fields are observed on the *x-z* plane at $y = 0$. When the *Z-thickness* is small, the coupling between top and bottom of surface charges becomes strong, therefore, shape variation becomes sensitive. To verify the phase difference due to fabrication errors, the *X-length and* the *Y-length* increase

and decrease by ±5 nm from the original parameter for patterns (a), (b), and (c). Figure 10 shows the combinations of the antenna length which can maintain the phases difference 90° ±5°, where the ideal circularly polarized light can be exactly achieved when the phase difference is 90°. The number of possible combinations is 7 for pattern (a), 14 for pattern (b), and 37 for pattern (c). Therefore, the *Z-thickness* =60nm is the most robust.

3.2 Control for polarization of localized light using a symmetric antenna model

The plasmonic antenna shown in Figure 11 is symmetric along both x and y axes. Compared with the original antenna indicated by the red line, the size of the antenna components placed along the x axis is 5 nm bigger in terms of both length and width.

Figure 12 shows the distribution of C'. The observation plane is sliced at the center of the particle recording media. Figure 12 (a) is the plot obtained when the incident light is linearly polarized. As the shape is slightly different from the original model, the circularity C' in the target medium is less than 1.0, i.e., the polarization turns elliptical. Figure 12 (b) is the same plot when the incident polarization is designed using the proposed method. The circularity C' can be improved and circular polarization is obtained.

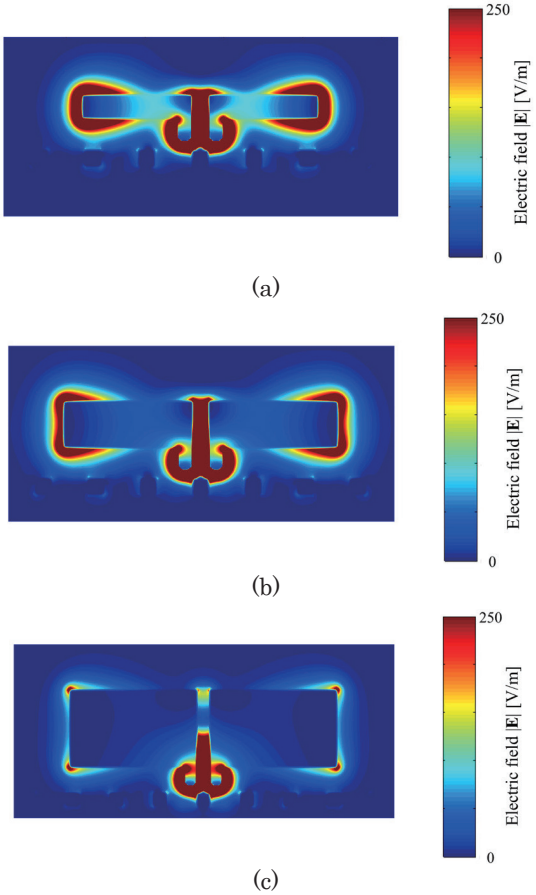

Fig. 9 Electric field around plasmonic antenna on x-z plane at y = 0 for patterns (a), (b), and (c).

3.3 Control for polarization of localized light using an asymmetric antenna model

Figure 13 is an example of the asymmetric antenna model: the size of the right-hand antenna portion is slightly modified and enlarged by 5 nm in terms of both length and width. The size of the left-hand antenna portion is the same as that of the original one.

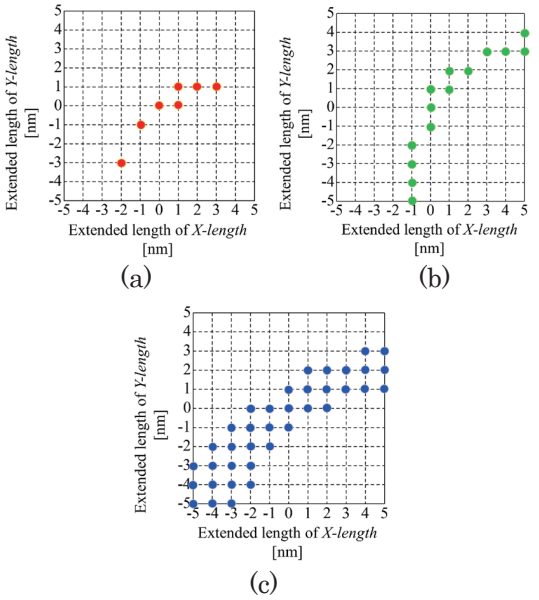

Fig. 10 Possible combinations of antenna length that can maintain 90° ± 5° phase difference. (a) *Z-thickness* = 15 nm, (b) *Z-thickness* = 30 nm, and (c) *Z-thickness* = 60 nm

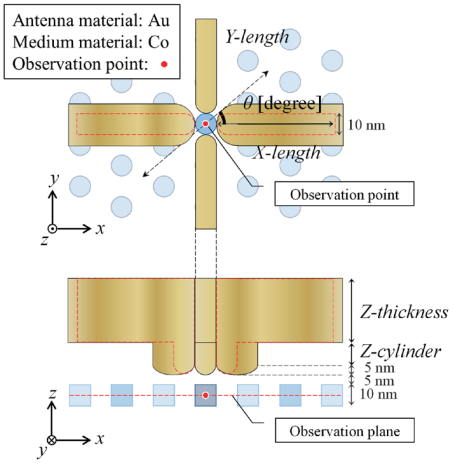

Fig. 11 Symmetric antenna model.

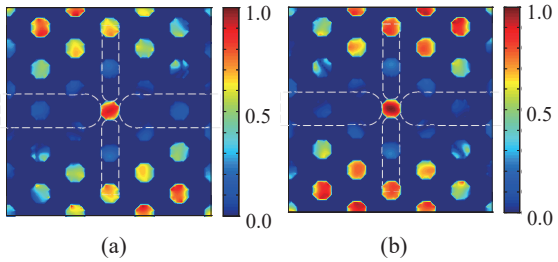

Fig. 12 Distribution of circularity C' for symmetric antenna model.

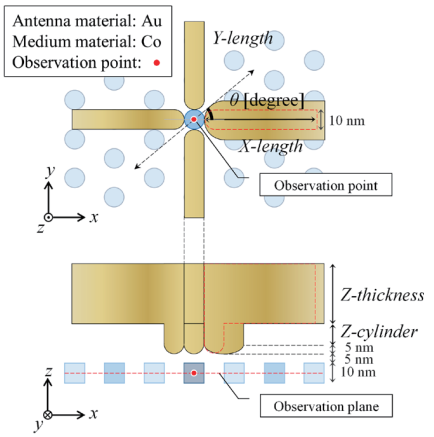

Fig. 13 Asymmetric antenna model.

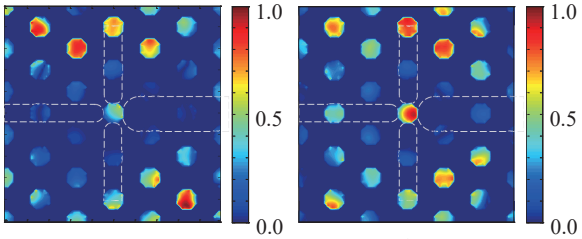

Fig. 14 Distribution of circularity C' for asymmetric antenna model.

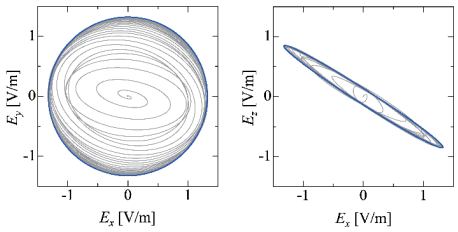

Fig. 15 Lissajous plot of electric field component for asymmetric antenna model.

Figure 14 (a) shows the degree of circular polarization C' when the incident light is linearly polarized. Owing to the antenna's asymmetry, the circularity C' decreases and is less than 1.0. Figure 14 (b) shows the computational result when the incident light is designed via the proposed method. The circularity C' inside the target medium is still 0.83. Although the circularity C' is improved for this asymmetric model, the polarization is still elliptical. To clarify the reason, we study all the electric components, as shown in Figure 15. The Lissajous plot indicates that the circular locus is obtained for E_x – E_y; however, the E_x – E_z locus is elliptical. Therefore, we conclude that the circularity C' decreases owing to the existence of the E_z component.

To overcome the problem of the asymmetric antenna model, we propose another method to generate localized circular light. In this method, C' is less than one because the E_z component exists. Therefore, we assume that the incident plane is inclined to omit the E_z component, as shown in Figure 16. When we selected the angle φ to be 45°, the circularly polarized light could be generated as

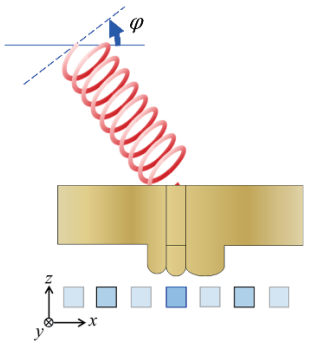

Fig. 16 Inclined incident plane used to omit E_z component.

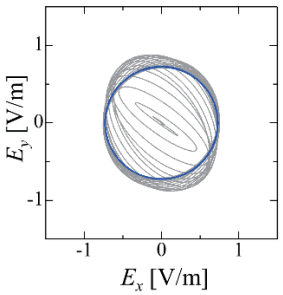

Fig. 17 Lissajous plot of electric field component by inclined incident plane.

Table 3 Electric field E_z and circularity C' for each incident wave.

φ (°)	0	45
E_z/E_x	0.65	0.36
C''	0.83	0.94

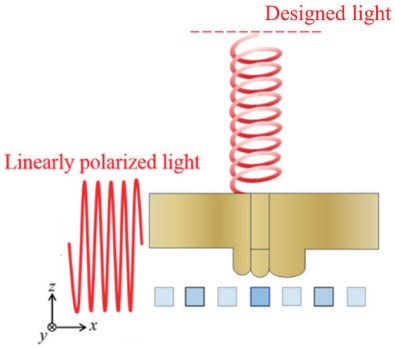

Fig. 18 Improvement to asymmetric antenna model's circularity.

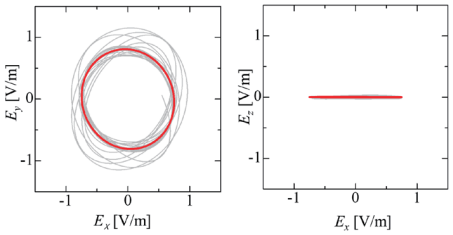

Fig. 19 Lissajous plot of electric field component for asymmetric antenna model.

shown in Figure 17. The circularity further improves from 0.83 to 0.94, and the E_z component decreases, as shown in Table 3.

3.4 Improvement of circularity for an asymmetric antenna

The designed incident light can improve the circularity C' for the asymmetric antenna. However, as the generated electric field in particle recording media has a z component, C' decreases. It can be improved by two incident waves: the designed incident wave and the electric field with z component propagated toward the x component, as shown in Figure 18. Figure 19 shows the Lissajous plot of the electric field component. The electric field of the x and y components is circular. The electric field of the x and z components is linear, and the z component vanishes. In this case, $C' = 1$ can be obtained.

4. Conclusion

The robustness of antenna shape against fabrication error was investigated. High-intensity circularly polarized light can be generated by increasing the antenna thickness, and it has high robustness. Furthermore, the proposed control method for the amplitude and phase of the localized light generated by plasmonic antennas can be successfully applied to the arbitrary shapes of plasmonic antennas, and any polarization of localized light can be produced. This method is very useful for developing ultra-fast magnetic recording systems.

Acknowledgments This work was partly supported by a Grant-in-Aid for Scientific Research (C) (17K06401) and the Nihon University College of Science and Technology Project for Research.

References

1) C. D. Stanciu, F. Hansteen, A. V. Kimel, A. Kirilyuk, A. Tsukamoto, A. Itoh, and T. Rasing: *Phys. Rev. Lett.*, **99**, 047601 (2007).
2) I. Radu, K. Vahaplar, C. Stamm, T. Kachel, N. Pontius, H. A. Dürr, T. A. Ostler, J. Barker, R. F. L. Evans, R. W. Chantrell, A. Tsukamoto, A. Itoh, A. Kirilyuk, Th. Rasing, and A. V. Kimel: *Nature*, **472**, 205 (2011).
3) C-H. Lambert, S. Mangin, B. S. D. Ch. S. Varaprasad, Y. K. Takahashi, M. Hehn, M. Cinchetti, G. Malinowski, K. Hono, Y. Fainman, M. Aeschlimann, and E. E. Fullerton: *Science*, **345**, 1337 (2014).
4) S. Mangin, M. Gottwald, C-H. Lambert, D. Steil, V. Uhlír, L. Pang, M. Hehn, S. Alebrand, M. Cinchetti, G. Malinowski, Y. Fainman, M. Aeschlimann, and E. E. Fullerton: *Nature Mat.*, **13**, 286 (2014).
5) M. Beens, M. L. M. Lalieu, A. J. M. Deenen, R. A. Duine, and B. Koopmans: *Phys. Rev. B*, **100**, 220409(R) (2019).
6) K. Nakagawa, Y. Ashizawa, S. Ohnuki, A. Itoh, and A. Tsukamoto: *J. Appl. Phys.*, **109**, 07B735 (2011).
7) T. Ota, Y. Ashizawa, K. Nakagawa, S. Ohnuki, H. Iwamatsu, A. Tsukamoto, and A. Itoh: *J. Magn. Soc. Jpn.*, **36**, 660 (2012).
8) B. Koene, M. Savoini, A. V. Kimel, A. Kirilyuk, and T. Rasing: *Appl. Phys. Lett.*, **101**, 013115 (2012).
9) K. Tamura, T. Ota, Y. Ashizawa, A. Tsukamoto, A. Itoh, S. Ohnuki, and K. Nakagawa: *J. Magn. Soc. Jpn.*, **37**, 115 (2013).
10) S. Ohnuki, K. Tatsuzawa, Y. Takano, Y. Ashizawa, and K. Nakagawa: *Adv. Intel. Syst. Comput.*, **387**, Springer (2015).
11) S. Kishimoto, T. Okada, S. Ohnuki, Y. Ashizawa, and K. Nakagawa: *Prog. Electromagn. Res.*, **146**, 155 (2014).
12) T. Yamaguchi and T. Hinata: *Opt. Express*, **15**, 11481 (2007).
13) A. Taflove and S. C. Hagness: *Computational Electrodynamics,* Third ed., p. 361 (Artech House, Norwood, MA, USA, 2005).
14) S. Ohnuki, T. Kato, Y. Takano, Y. Ashizawa, and K. Nakagawa: *Radio Sci.*, **50**, 29 (2015).
15) P. Biagioni, J. S. Huang, L. Duò, M. Finazzi, and B. Hecht: *Phys. Rev. Lett.*, **102**, 256801 (2009).
16) P. Biagioni, M. Savoini, J.-S. Huang, L. Duò, M. Finazzi, and B. Hecht: *Phys. Rev. B*, **80**, 153409 (2009).

Received Jan. 10, 2020; Revised Mar. 07, 2020; Accepted Apr. 19, 2020

J. Magn. Soc. Jpn., **44**, 102-107 (2020)

<Paper>

Decomposition of Magnetic Field Intensity in Ferrite Based on Time Derivative of Magnetic Flux Density and Power Loss

Hideo Saotome and Tatsuki Washizu

Graduate School of Engineering, Chiba University, *1-33 Yayoi-cho, Inage-ku, Chiba 263-8522, Japan*

A method for the power loss analysis for ferrite is required and is expected to lead to the development of low-loss ferrites. In the present paper, the magnetic field intensity in ferrite was decomposed into four components for the analysis. When the time derivative of the magnetic induction, dB/dt, is low, the magnetic field intensity is composed of only two components, H_u and H_h, which yield the magnetic flux and the hysteresis loss, respectively. At high-dB/dt excitations, magnetic field intensities, H_v and H_f, appear in addition to H_u and H_h, where H_v lowers the permeability and H_f causes the dynamic magnetic loss, respectively. The temperature characteristics of H_u, H_h, H_v and H_f differ, which implies that the hysteresis and dynamic magnetic losses are caused by different physical mechanisms. The function tables for H_u (B, B_m), H_h (B, B_m), H_v (B, dB/dt, B_m) and H_f (B, dB/dt, B_m) were obtained from measurements conducted at ferrite core temperatures of 20, 40, and 60 °C, where B_m is the maximum magnetic flux density. The tables were used to simulate the magnetic field intensity for the excitation when a sinusoidal waveform voltage was applied to a ferrite inductor. The simulation results show good agreement with the experimental results.

Key words: ferrite, iron loss, hysteresis loss, dynamic magnetic loss, temperature

1. Introduction

Ferrite is widely used for high-frequency transformers, especially those in DC–DC converters. The iron loss in ferrite is well known to increase with increasing excitation frequency, i.e., the time derivative of the magnetic flux density, dB/dt. The B–H loop, where H is the magnetic field intensity, broadens with increasing dB/dt for a given maximum value of the magnetic flux density. The area inside the B–H loop can be divided into two components corresponding to the hysteresis loss and the residual loss [1]. In the case of electrical steel sheets, the iron loss was divided into three components; the hysteresis loss, the eddy current loss and the residual loss. Their separation was carried out based on the difference of their frequency characteristics [2]. As for the analysis of the residual loss in electrical steel sheets, the anomalous eddy current caused by magnetic domain wall movement was proposed [3]. In ferrite, the dynamic magnetic loss accounts for most of the residual loss [4]. The assumption that the residual loss is due to eddy-current losses in a ferrite core body, grains, and/or magnetic domains is inconsistent with experimental results [5].

The purpose of the present study is to develop a precise ferrite magnetization model that includes the dynamic magnetic power loss. The model comprises the instantaneous values of four magnetic field intensities given by the magnetic flux density, B, its time derivative, dB/dt, and the maximum magnetic flux density, B_m, for the excitation. Each of the magnetic field intensities depends on the ferrite temperature, T. When a ferrite core is excited, such as by a rectangular or sinusoidal waveform voltage, its power loss can be estimated with the model. The validity of the model proposed in this paper is verified quantitatively by comparing the simulated results with the experimental results under a sinusoidal waveform voltage excitation, where dB/dt changes at every moment, along with the voltage. The proposed model is expected to contribute not only to the power loss estimations of power electronics circuits with ferrite-applied devices, but also to the development of low loss ferrites at given dB/dt, B_m and T.

2. Decomposition of magnetic field intensity

Our experiments on ferrite PC47 (TDK Corporation [6]) have shown that the shape of its B–H loops does not change when dB/dt is less than approximately 5 mT/μs, even when it is excited by different waveform voltages of the same volt-second value. Similar phenomena have been observed in the hysteresis loops for electrical steel sheets at very low excitation frequencies such as 10 Hz or less [7, 8].

The magnetic field intensity obtained under low-dB/dt excitation consists of two components, H_u and H_h, as shown in Fig. 1(a), where H_u and H_h generate the magnetic flux and the hysteresis loss, respectively. The H_u curve passes through the center of the B–H loop and H_h is the distance from the center to the edge of the B–H loop, as shown in Fig. 1(a). H_u and H_h are functions of B and B_m, where B_m is given by the volt-second value of the excitation voltage. For excitations greater than 100 mT/μs at dB/dt, the B–H loops become markedly wider, as shown

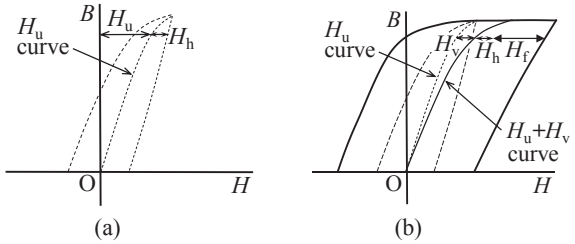

Fig. 1 B-H curves at (a) low dB/dt and (b) high dB/dt.

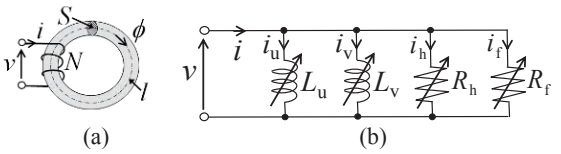

Fig. 2 Ferrite inductor and its equivalent circuit without winding resistance: (a) Inductor and (b) equivalent circuit.

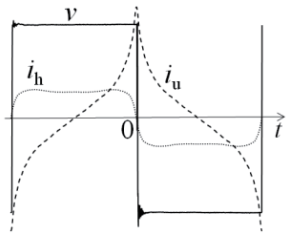

Fig. 3 Current waveforms excited by a rectangular waveform voltage at low dB/dt.

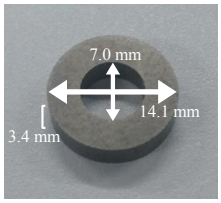

Fig. 4 Toroidal core (TDK PC47) used in experiments.

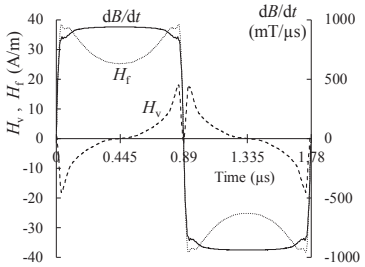

Fig. 5 H_v and H_f waveforms excited at dB/dt = 900 (mT/μs), B_m = 400 (mT) and T = 20 (°C).

by the solid lines in Fig. 1(b), than those under low-dB/dt conditions. The magnetic field intensity H_f generates the dynamic magnetic loss. Under high-dB/dt excitations, the slope of the B–H loop is slightly gentler than that for the low-dB/dt case; thus, the center curve, H_u + H_v, has a slightly gentler slope than the H_u curve. This decrease in slope means that the effective permeability decreases with increasing dB/dt. That is, in addition to H_u, H_v is needed to attain the same value of B as in the cases under the low-dB/dt condition. H_v and H_f are functions of B, dB/dt, and B_m.

Applying Ampere's law to H_u, H_h, H_v, H_f and their sum, H, in the core shown in Fig. 2(a), we obtain their corresponding excitation currents:

$$i_u = (l/N)\,H_u, \quad (1)$$

$$i_h = (l/N)\,H_h, \quad (2)$$

$$i_v = (l/N)\,H_v, \quad (3)$$

$$i_f = (l/N)\,H_f, \quad (4)$$

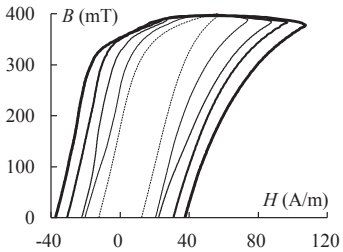

Fig. 6 B-H loops at dB/dt = 5, 300, 500, 700 and 900 (mT/μs), in ascending order of the magnetic field intensity; and T = 20 (°C).

$$i = (l/N)\,H, \quad (5)$$

where N and l are the number of turns and the magnetic flux path length, respectively. These currents are assumed to flow in the equivalent circuit of the inductor, as shown in Fig. 2(b). Excitation currents i_u and i_v flow in inductors L_u and L_v, respectively, because they contribute to generating the magnetic flux without power loss. However, i_h and i_f flow in resistors R_h and R_f, respectively, because they contribute to yielding the power loss without storing magnetic energy in the ferrite inductor shown in Fig. 2(a).

In the case of low-dB/dt excitation (e.g., 5 mT/μs), only i_u and i_h flow in the equivalent circuit, where i_u and i_h are in phase with the magnetic flux, ϕ, and the applied voltage, v, respectively, shown in Fig. 2(a). The relation between ϕ and v is well-known as

$$v = N\,(\mathrm{d}\phi/\mathrm{d}t) = N\,S\,(\mathrm{d}B/\mathrm{d}t), \quad (6)$$

where S is the cross-sectional area of the magnetic flux path of the core shown in Fig. 2(a). Applying a rectangular waveform voltage to the core, we obtain the waveforms of i_u and i_h, as depicted in Fig. 3. When the excitation current, i, is measured, applying a Fourier series to it gives i_u and i_h because i_u and i_h are the even and odd functions with respect to t = 0, respectively. In a high-dB/dt excitation case, i_v and i_f are added to i_u and i_h in i. Similar to i_u and i_h, i_v and i_f are in phase with ϕ and v, respectively. When dB/dt = 900 (mT/μs) is applied to the core (Fig. 4), the waveforms of H_v and H_f are obtained from the measured i, as shown in Fig. 5, where B_m = 400 (mT), which is given by integrating dB/dt for one-quarter of the period. The experiment giving Fig. 5 was carried out when core temperature T was controlled at 20 °C. H_v and H_f were computed by subtracting H_u and H_h from H and applying a Fourier series to the remainder, where H_u and H_h were obtained from i_u and i_h measured at low-dB/dt excitation and at B_m = 400 (mT).

Figure 6 shows B–H loops of different dB/dt values at T = 20 (°C). The largest loop is measured at dB/dt = 900 (mT/μs), and the smallest one at dB/dt = 5 (mT/μs), corresponding to Fig. 1(a). Other loops are measured at 300, 500 and 700 mT/μs. Figure 6 shows that increasing dB/dt causes not only an increase in the area of B–H loops but also changes their slopes, as previously described. In the present paper, the loop shown by dotted lines in Figs. 1 and 6 is called the hysteresis loop to distinguish it from the B–H loops given by high-dB/dt excitations.

In Fig. 5 showing experimental results, H_v becomes small near B_m, i.e., the time interval when dB/dt changes its polarity, because the waveform of dB/dt is not ideal as a rectangular waveform. The magnetic flux density still increases very little during the time interval as long as dB/dt is positive. That is, the maximum value of the magnetic field intensity, H_m, does not correspond to B_m. B_m occurs after H_m, as shown in Fig. 6. Ideally, H_v should be measured by applying an ideal rectangular waveform voltage; H_v then maintains a proper value near B_m.

In summary, the measurements under low-dB/dt excitation give H_u and H_h, which are separated using a Fourier series, and the measurements under the high-dB/dt excitation give H_v and H_f, which are also separated using a Fourier series. The boundary of the low-dB/dt and high-dB/dt is determined on the basis of the hysteresis loop, which is independent of dB/dt. The excitation currents given by Eqs. (1)–(5) and illustrated in Fig. 2(b) lead to the H_u, H_h, H_v and H_f values shown in Figs. 1(a) and (b). From a power-loss analysis viewpoint, the instantaneous values of the hysteresis and dynamic magnetic losses, p_h (W/m^3) and p_f (W/m^3), can be calculated by

$$p_h = H_h\,(\mathrm{d}B/\mathrm{d}t), \quad (7)$$

$$p_f = H_f\,(\mathrm{d}B/\mathrm{d}t), \quad (8)$$

respectively, because both of H_h and H_f, i.e., i_h and i_f, are in phase with dB/dt and v.

3. Availability of the decomposition

The four introduced magnetic field components, H_u, H_h, H_v and H_f are temperature dependent. In this section, we show some examples of the experimental results at $T = 40$ (°C). To construct the function tables $H_u(B, B_m)$, $H_h(B, B_m)$, $H_v(B, \mathrm{d}B/\mathrm{d}t, B_m)$ and H_f (B, dB/dt, B_m), measurements of H with respect to B, dB/dt, and B_m were carried out by rectangular waveform voltage excitations for $B_m = 50$, 100, 150, 200, 250, 300, 350 and 400 (mT), and dB/dt = 5, 40, 80, 130, 200, 300, 400, 500, 700 and 900 (mT/μs). Several measured data are shown in Fig. 7, where $B_m = 200$ (mT). The dotted line in Fig. 7(a) shows the hysteresis loop given at dB/dt = 5 (mT/μs). The hysteresis loop in Fig. 7(a) keeps its shape and size even when excited at dB/dt = 1 (mT/μs) and the same B_m. The dotted line shown in Fig. 7(b) is the H_u curve (H_v = 0) obtained from the hysteresis loop in Fig. 7(a). Figure 7(c) shows H_h with respect to B. Whereas H_u and H_h are independent of dB/dt, H_v and H_f are dependent on it. Figure 7(b) shows that increasing dB/dt results in an increase of H_v and that, as a result, the $H_u + H_v$ curve leans to the right. H_f increases with increasing dB/dt, as shown in Fig. 7(d). The dynamic magnetic loss defined by Eq. (8), which corresponds to the area surrounded by the B–H_f loops in Fig. 7(d), increases with increasing dB/dt, whereas the area surrounded by the B–H_h loop in Fig. 7(c) is constant as long as B_m is fixed. The function tables $H_u(B, B_m)$, $H_h(B, B_m)$, $H_v(B, \mathrm{d}B/\mathrm{d}t, B_m)$ and H_f (B, dB/dt, B_m) were completed with the measured data, similar to the results presented in Fig. 7.

When rectangular waveform dB/dt is applied,

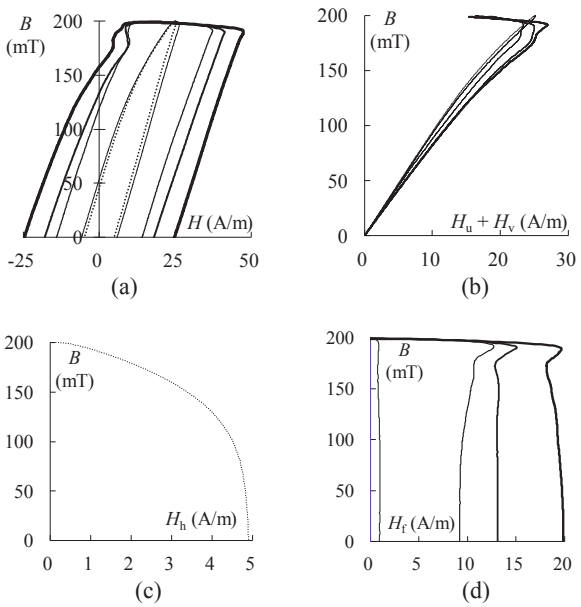

Fig. 7 H, $H_u + H_v$, H_h and H_f versus B when $B_m = 200$ (mT) and $T = 40$ (°C). The dotted lines in (a), (b) and (c) are at dB/dt = 5 (mT/μs). The solid lines in (a), (b) and (d) are at dB/dt = 40, 400, 500 and 700 (mT/μs), respectively, in ascending order of the magnetic field intensities.

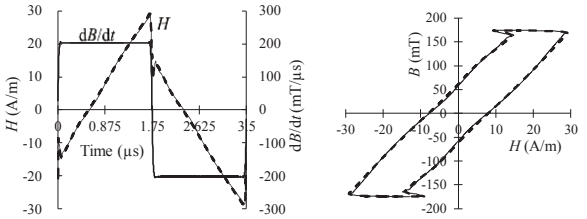

Fig. 8 Comparisons of experimental and simulated results under the rectangular waveform voltage excitation when $B_m = 175$ (mT) and $T = 40$ (°C): (a) Time waveforms and (b) B-H loops. The solid and broken lines show the experimental and simulated results, respectively.

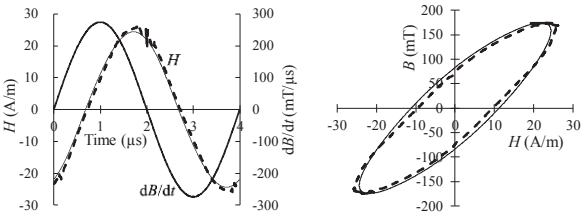

Fig. 9 Comparisons of experimental and simulated results under the sinusoidal waveform voltage excitation when $B_m = 175$ (mT) and $T = 40$ (°C): (a) Time waveforms and (b) B-H loops. The solid and broken lines show the experimental and simulated results, respectively.

$$H = H_u + H_h + H_v + H_f \quad (9)$$

can be calculated with the function tables. Figure 8 shows the computed and experimentally obtained H with respect to time, and their corresponding B–H loops. The excitation conditions of dB/dt and B_m were 200 mT/μs and 175 mT, respectively, where 175 mT was not the condition for the measured data listed in the tables. The simulated results are consistent with the experimental data, indicating that the interpolation functions used in the computations are suitable. When dB/dt was sinusoidally changed, H and its B–H loop were calculated and compared with the experimental results, as shown in Fig. 9. The reproducibility of the B–H loops obtained using the function tables is also verified. Figures 8 and 9 show that the magnetization characteristic $H_u(B, B_m)$, $H_h(B, B_m)$, $H_v(B, dB/dt, B_m)$ and $H_f(B, dB/dt, B_m)$ are the essential magnetic properties for ferrite and that the ferrite power loss can be estimated using them when dB/dt is specified or given. The decomposition of the magnetic field intensities introduced in this paper is useful to simulate the power losses of magnetic cores in power electronics circuits and is expected to contribute to the development of high-efficiency converters.

4. Temperature dependence

As previously mentioned, $H_u(B, B_m)$, $H_h(B, B_m)$, $H_v(B, dB/dt, B_m)$ and $H_f(B, dB/dt, B_m)$ are temperature dependent. Figures 10(a) and 10(b) show the experimental results for the temperature dependence of H_h and H_f, respectively, where dB/dt was fixed at (a) 5 mT/μs and (b) 400 mT/μs with rectangular waveform voltage excitations and B_m = 300 (mT). Whereas H_f remains almost unchanged, H_h decreases with increasing temperature. The temperature characteristics of H_v differ from those of H_u, as shown in Figs. 11(a) and 11(b), where the excitation conditions are the same as those corresponding to Fig. 10. Whereas H_u increases with increasing temperature, H_v decreases. Figures 12(a) and 12(b) show the temperature characteristics of H_h and H_f, respectively, excited at B_m = 400 (mT), where dB/dt = 900 (mT/μs) for Fig. 12(b). The temperature characteristics of H_h shown in Figs. 10(a) and 12(a) are consistent. However, the correlation of these characteristics for H_f between Figs. 10(b) and 12(b) is not observed. Figures 13(a) and 13(b) show the temperature characteristics of H_u and H_v, respectively, excited at B_m = 400 (mT), where dB/dt = 900 (mT/μs) for Fig. 13(b). The temperature characteristics of H_u in Fig. 13(a) are similar to those in Fig. 11(a); that is, H_u increases with increasing temperature. However, the temperature characteristics of H_v in Figs. 11(b) and 13(b) are not consistent. The experimental results in Figs. 10, 11, 12 and 13 at least clarify that H_u and H_h both exhibit the nature of a law on temperature dependence, whereas H_v and H_f do not, at least at the temperature resolution shown in this paper. The difference in temperature dependence between H_f and H_h suggests that the dynamic magnetic loss related to H_f and expressed by Eq. (8) is caused by magnetization (or electron spin) other than the one that causes the hysteresis loss and H_h.

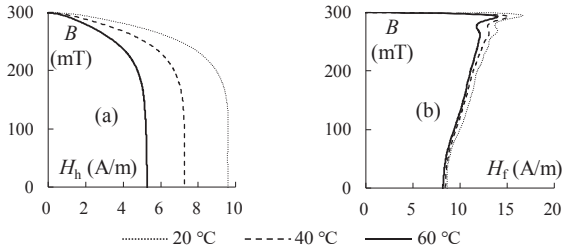

Fig. 10 Temperature characteristics of (a) H_h and (b) H_f excited at B_m = 300 (mT): (a) dB/dt = 5 (mT/μs) and (b) dB/dt = 400 (mT/μs).

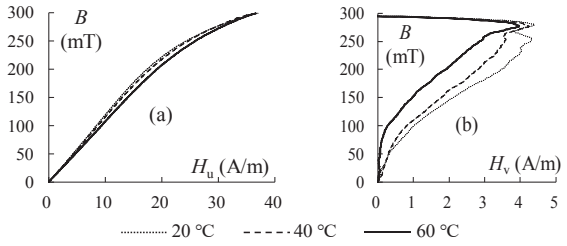

Fig. 11 Temperature characteristics of (a) H_u and (b) H_v excited at B_m = 300 (mT): (a) dB/dt = 5 (mT/μs) and (b) dB/dt = 400 (mT/μs).

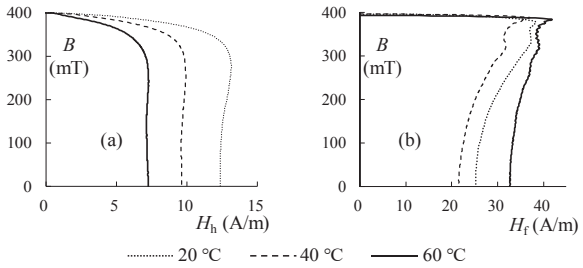

Fig. 12 Temperature characteristics of (a) H_h and (b) H_f excited at B_m = 400 (mT): (a) dB/dt = 5 (mT/μs) and (b) dB/dt = 900 (mT/μs).

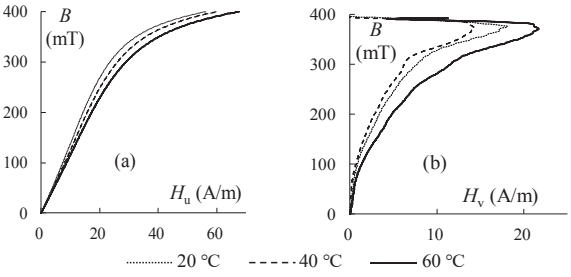

Fig. 13 Temperature characteristics of (a) H_u and (b) H_v excited at B_m = 400 (mT): (a) dB/dt = 5 (mT/μs) and (b) dB/dt = 900 (mT/μs).

Ferrite catalogs give the temperature characteristics of power losses [6], however, their values are not shown by discriminating the hysteresis loss and the dynamic magnetic loss. As shown in Figs. 10 and 12, the blending ratios of compounds for ferrites can be evaluated by

separating the hysteresis and dynamic magnetic losses. The proposed magnetic field separation can be used to improve the manufacturing of low-loss ferrite, especially at high-dB/dt excitation.

5. Discussion

Figures 14(a) and 14(b) show experimentally obtained $H_u + H_v$ curves at dB/dt = 5, 300, 700 and 900 (mT/μs). The ferrite core body temperatures corresponding to the figures are (a) 20 °C and (b) 60 °C. The results show that the $H_u + H_v$ curves lean to the right (i.e., H_v increases) with increasing dB/dt. That is, H_v is reasonably assumed to be caused by demagnetization in the ferrite at high-dB/dt excitation because the effective permeability decreases. This fact suggests that the magnetization vector in ferrite, $\boldsymbol{M}$, is composed of two magnetization vectors, $\boldsymbol{M'}$ and $\boldsymbol{M''}$, shown in Fig. 15, i.e.,

$$\boldsymbol{M} = \boldsymbol{M'} + \boldsymbol{M''}, \tag{10}$$

where $\boldsymbol{M'}$ and $\boldsymbol{M''}$ play individual roles in magnetization and/or demagnetization. They rotate in synchronization with the magnetic field. With increasing dB/dt, the differential angle between $\boldsymbol{M'}$ and $\boldsymbol{M''}$ increases, as shown in Figs. 15(a) and 15(b); as a result, $\boldsymbol{M}$ decreases. Assuming that the torque for $\boldsymbol{M'}$ is much greater than that for $\boldsymbol{M''}$ at low-dB/dt excitation, $\boldsymbol{M'}$ is considered to cause the hysteresis loss defined by Eq. (7). On the other hand, at high-dB/dt excitation, $\boldsymbol{M''}$ is considered to yield the dynamic magnetic loss defined by Eq. (8).

In the case of electron spin and magnetization, the physical mechanisms of their functions of storing and consuming energy are assumed to differ. The fact that the dynamic magnetic loss increases with increasing

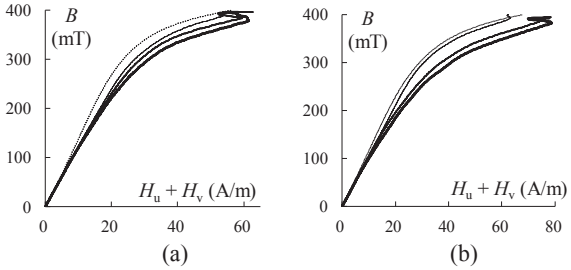

Fig. 14 $H_u + H_v$ curves at dB/dt = 5, 300, 700 and 900 (mT/μs), in ascending order of the magnetic field intensities: (a) 20 °C and (b) 60 °C.

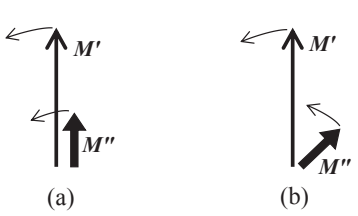

Fig. 15 The magnetization vector, $\boldsymbol{M}$, in ferrite is composed of $\boldsymbol{M'}$ and $\boldsymbol{M''}$, i.e., $\boldsymbol{M} = \boldsymbol{M'} + \boldsymbol{M''}$, where $\boldsymbol{M'}$ rotates owing to the applied magnetic field; $\boldsymbol{M''}$ is synchronized with $\boldsymbol{M'}$. (a) Low-dB/dt and (b) $\boldsymbol{M''}$ delays and results in demagnetization at high dB/dt.

Table 1 Dependence of $\boldsymbol{M'}$ and $\boldsymbol{M''}$ on temperature rise.

Magnetic energy	Corresponding physical variable for $\boldsymbol{M'}$ or $\boldsymbol{M''}$	$\boldsymbol{M'}$	$\boldsymbol{M''}$
Storage	Amplitude	Decrease	Not clear
Consumption	Average torque for a rotation	Decrease	Not clear

dB/dt suggests that the average torque for a rotation of $\boldsymbol{M''}$ strongly depends on the value of dB/dt, whereas the torque for $\boldsymbol{M'}$ does not. Although the demagnetization at high dB/dt is an experimental fact, the cause of $\boldsymbol{M''}$ remains unclear.

The dependence of $\boldsymbol{M'}$ and $\boldsymbol{M''}$ on the increase in temperature is summarized in Table 1. From Figs. 11(a), 13(a), 14 and other measured data mentioned in section 3, H_u is clarified to increase with increasing temperature for the same B. In other words, B decreases with increasing temperature when H_u is fixed. Assuming $|\boldsymbol{M''}| \ll |\boldsymbol{M'}|$, the amplitude of $\boldsymbol{M'}$ decreases with the temperature rise. From Figs. 10(a), 12(a) and other experimental data, H_h is clarified to decrease with increasing temperature. A portion of the torque for $\boldsymbol{M}$ contributes to storage of the magnetic energy, and the rest yields the power loss. Hence, the average value of the torque for one period of the vector rotation contributes to the magnetic energy consumption. The torque of $\boldsymbol{M'}$ used for the hysteresis loss decreases with increasing temperature. In the case of $\boldsymbol{M''}$, we could not find any tendency with respect to the temperature rise. However, the difference of the temperature characteristics between $\boldsymbol{M'}$ and $\boldsymbol{M''}$ is very clear.

6. Conclusion

The magnetic property in ferrite was analyzed by deconvoluting the magnetic field into four components. The deconvolution was carried out on the basis of the value of dB/dt and whether the magnetic field contributes to magnetic energy storage or consumption.

An equivalent circuit model for a ferrite inductor was proposed using the deconvoluted magnetic fields. Excitation currents of a ferrite inductor can be estimated with this model. Applying the model to the analysis of power electronic circuits enables improvements in their efficiencies.

The power loss in ferrite was divided into two parts, i.e., the hysteresis and dynamic magnetic losses. With the power loss separation proposed in this paper, novel developments of low-loss ferrite can evolve.

Some hypothetical considerations regarding the magnetization vectors in ferrite were described on the basis of the difference in the temperature characteristics between the hysteresis and dynamic magnetic losses and the reduction of the permeability at high dB/dt.

References

1) S. Chikazumi: Physics of Ferromagnetism, Vol.II, Magnetic Characteristics and Engineering Application, (in Japanese), (Syokabo, Tokyo, 1984).
2) https://www.iti.iwatsu.co.jp/ja/products/sy/pdf/011_B-H_analyzer_FAQ_A18-v02.pdf, as of May 11, 2020.
3) C. Kaido, *J. Magn. Soc. Jpn.*, **33**, 144(2009).
4) H. Saotome and Y. Sakaki: *IEEE Trans. Magn.*, **33**, 728 (1997).
5) H. Saotome, *J. Magn. Soc. Jpn.*, **40**, 19(2016).
6) https://product.tdk.com/info/ja/catalog/datasheets/ferrite_mn-zn_material_characteristics_ja.pdf, as of May 11, 2020.
7) T. Matsuo and M. Shimasaki: *IEEE Trans. Magn.*, **41**, 3112(2005).
8) https://www.jfe-steel.co.jp/products/denji/catalog/f2j-001.pdf, as of May 11, 2020.

Received Apr. 16, 2020; Revised May 11, 2020; Accepted May 13, 2020

Journal of the Magnetics Society of Japan

Vol. 44 No. 4 (通巻第 310号) 2020年7月1日発行

Vol. 44 No. 4 Published Jul. 1, 2020
by the Magnetics Society of Japan
Tokyo YWCA building Rm207, 1–8–11 Kanda surugadai, Chiyoda-ku, Tokyo 101–0062
Tel. +81–3–5281–0106 Fax. +81–3–5281–0107

Printed by JP Corporation Co., Ltd.
Sports Plaza building 401, 2–4–3, Shinkamata Ota-ku, Tokyo 144–0054
Advertising agency: Kagaku Gijutsu-sha

発行：（公社）日本磁気学会 101–0062 東京都千代田区神田駿河台 1–8–11 東京YWCA会館 207 号室
製作：ジェイピーシー 144–0054 東京都大田区新蒲田 2–4–3 スポーツプラザビル401 Tel.（03）6715–7915
広告取扱い：科学技術社 111–0052 東京都台東区柳橋 2–10–8 武田ビル 4F Tel.（03）5809–1132